Stochastic series expansion algorithm for the $S=1/2$ XY model with four-site ring exchange

Roger G. Melko[1] and Anders W. Sandvik[2]
[1]*Department of Physics, University of California, Santa Barbara, California 93106, USA*
[2]*Department of Physics, Boston University, 590 Commonwealth Avenue, Boston, Massachusetts 02215, USA*
(Received 5 September 2004; revised manuscript received 13 May 2005; published 10 August 2005)

We describe a stochastic series expansion quantum Monte Carlo method for a two-dimensional $S=1/2$ XY model (or, equivalently, hard-core bosons at half filling) which in addition to the standard pair interaction J includes a four-site term K that flips spins on a square plaquette. The model has three ordered ground state phases; for $K/J \lesssim 8$ it has long-range xy spin order (superfluid bosons), for $K/J \gtrsim 15$ it has staggered spin order in the z direction (charge-density wave), and between these phases it is in a state with columnar order in the bond and plaquette energy densities. We discuss an implementation of directed-loop updates for the SSE simulations of this model and also introduce a "multibranch" cluster update which significantly reduces the autocorrelation times for large K/J. In addition to the pure J-K model, which in the z basis has only off-diagonal terms, we also discuss modifications of the algorithm needed when various diagonal interactions are included.

DOI: 10.1103/PhysRevE.72.026702 PACS number(s): 05.10.Ln, 05.30.−d, 75.10.−b, 75.40.Mg

I. INTRODUCTION

In the ongoing quest to explore possible ground states and quantum phase transitions in quantum condensed matter systems (fermions, bosons, or quantum spins), numerical studies are important for establishing the true nature of the phases and transitions of relevant model Hamiltonians. In particular, recent interest in "exotic" phenomena has focused attention on models with frustrated or competing interactions, in which interplay between adjacent ordered phases often gives rise to interesting effects [1–4]. For classical models, Monte Carlo simulations in combination with finite-size scaling can be used very successfully in studies of a wide range of systems with and without frustration. However, only a limited class of quantum models are amenable to such studies, as the infamous sign problem prohibits large-scale quantum Monte Carlo (QMC) studies of frustrated antiferromagnetic spin systems and fermions in more than one dimension. It is therefore important to search for non-sign-problematic quantum models, possibly with competing interactions, that display complex ground state phase diagrams and can be efficiently studied using Monte Carlo simulations. Although not all possible types of ground states and quantum phase transitions may be realizable within this class of Hamiltonians, it is likely that many insights into the low-temperature physics of quantum matter can still be gained in this way. Constructing optimized and efficient quantum Monte Carlo algorithms for such candidate Hamiltonians is hence an important task.

In this paper, we present the details of a stochastic series expansion (SSE) algorithm that we have developed for large-scale QMC studies of a two-dimensional (2D) $S=1/2$ XY model with an added four-site ring-exchange term (the method can be easily generalized for three-dimensional systems [5]). Defining the following bond and plaquette operators:

$$B_{ij} = S_i^+ S_j^- + S_i^- S_j^+ = 2(S_i^x S_j^x + S_i^y S_j^y), \tag{1}$$

$$P_{ijkl} = S_i^+ S_j^- S_k^+ S_l^- + S_i^- S_j^+ S_k^- S_l^+, \tag{2}$$

the J-K Hamiltonian is given by

$$H = -J \sum_{\langle ij \rangle} B_{ij} - K \sum_{\langle ijkl \rangle} P_{ijkl}, \tag{3}$$

where $\langle ij \rangle$ denotes a pair of nearest-neighbor sites on a 2D square lattice and $\langle ijkl \rangle$ are sites on the corners of a plaquette, as illustrated in Fig. 1(a). The plaquette flip P_{ijkl} is only a subset of all the possible cyclic exchanges among four spins and corresponds to retaining only the purely x and y terms; it has a nonvanishing matrix element only between the two spin states with alternating (staggered) spins on the corners of the plaquette, as illustrated in Fig. 1(b). In the standard way, the J-K Hamiltonian (3) can also be considered as a half-filled hard-core boson model, where up and down spins correspond to filled and empty sites and J is the nearest-neighbor hopping. We will frequently use terminology referring to this boson representation. With the negative sign in front of the plaquette term ($K>0$), the J-K model can be studied using QMC methods without a sign problem (the sign of the J term is actually irrelevant in this regard). In this model, there is no frustration in the conventional sense, i.e., antiferromagnetic interactions on lattice loops with an odd number of links (which leads to sign problems). However, the J and K terms individually favor different types of ground states, which leads to interesting competition effects at intermediate K/J.

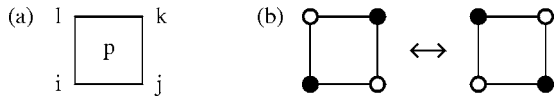

FIG. 1. (a) Labeling convention for the indices of an operator O_{ijkl} acting on the corners of a plaquette. The label p refers to the whole plaquette, so that $O_p \equiv O_{ijkl}$. (b) The two plaquette configurations between which the K term can act; open and solid circles correspond to up and down spins, respectively.

The J-K model was recently found to exhibit three different ordered ground states as a function of the ratio K/J of the four-site (K) and two-site (J) terms [6]. It was argued that the transition between the magnetically ordered state for $K/J \lesssim 8$ and a striped [or valence-bond-solid (VBS)] phase at higher K/J is a continuous quantum phase transition, contrary to general expectations for an order-order transition. Subsequently, this transition was proposed to possibly be a realization of a "deconfined" quantum critical point [1]. We have used the SSE algorithms to further study the quantum critical scaling and finite-T transitions in this model. However, in this paper we only briefly summarize the results and focus on the algorithmic issues. A full account of the results will be presented elsewhere [7].

For $K=0$, the J-K model reduces to the standard XY model, which undergoes a Kosterlitz-Thouless transition at $T_{\mathrm{KT}}/J \approx 0.69$ [8–10]. In the boson language, the system is a superfluid below T_{KT}. The main features of the $T=0$ phase diagram for $K/J>0$ were presented in Ref. [6]. Our most recent simulations [7] show that the superfluid density vanishes at $K/J \approx 7.91$. At the same point, within the accuracy of our calculations, the ground state develops a stripe order, where the bond and plaquette strengths $\langle B_{ij} \rangle$ and $\langle P_{ijkl} \rangle$ are modulated at wave vector $\mathbf{q}=(\pi,0)$ or $(0,\pi)$. This state can also be considered a columnar VBS, since not all the bonds within the "ladders" of strong bonds are equal—the strongest ones are those on the rungs of the ladders. The VBS order vanishes at $K/J \approx 14.5$, in a first-order transition to an Ising-type antiferromagnetic state [a charge-density wave (CDW) at $\mathbf{q}=(\pi,\pi)$ in the boson picture]. The nature of the superfluid-VBS transition has not yet been completely clarified. While we do observe power-law scaling with nontrivial exponents for the superfluid density as well as for the order parameter corresponding to the VBS phase, the exponents do not appear to be mutually consistent with hyperscaling. The transition could be weakly first order, but we do not have any direct evidence of discontinuities or of any region of coexistence of the two phases. Numerically we can of course never exclude an extremely weakly first-order transition or a very narrow coexistence region. We have also recently studied the evolution of the VBS phase boundaries when the system is coupled to an external magnetic field, and there we do find first-order transitions [11].

The outline of the rest of this paper is the following. In Sec. II we describe the SSE algorithm for the J-K Hamiltonian. Implementations of the SSE scheme for various spin [12,13] and 1D fermion [14] models have been discussed at length in several recent papers, but since the four-particle term necessitates a more complex sampling scheme, with some important additional features, we describe our algorithm in detail here. We have constructed two types of cluster updates for sampling the SSE configurations; a directed-loop update as well as a "multibranch" cluster update. The latter significantly reduces the autocorrelation times for large K/J. In Sec. II we also discuss estimators for several important physical quantities. We discuss autocorrelation functions in the different ordered phases in Sec. III. In Sec. IV we discuss modifications of the algorithm when different types of potential-energy terms are included in addition to the J and K terms. We conclude with a brief discussion in Sec. V.

II. STOCHASTIC SERIES EXPANSION

The SSE method [15–18] is an efficient and widely applicable generalization of Handscomb's [19] power-series method for the $S=1/2$ Heisenberg model. It has previously been used for several models with two-body interactions, including the pure XY model [$K=0$ in Eq. (3) [10]]. As in world-line Monte Carlo simulations [20], loop-cluster algorithms [21] can speed up SSE simulations very significantly [18,22]. Recently, a framework was devised for constructing and optimizing loop-type algorithms under very general conditions [12]. Here we will apply this *directed-loop* scheme to SSE simulations including the four-spin term. A loop-type algorithm cannot be constructed for the pure K model [$J=0$ in Eq. (3)], however, and the loops are also inefficient when $J/K \ll 1$. We therefore also develop a type of *multibranch* cluster update, which can be used in combination with the directed loops, and enables efficient simulations for any J/K. The multibranch update bears some resemblance to, but is more complex than, a "quantum-cluster" update recently developed for the transverse Ising model [13].

Below, we give a brief general summary of the SSE method. We then develop the directed-loop and multibranch cluster updates for the J-K Hamiltonian and discuss the SSE estimators of several important physical quantities. We present some illustrative results for autocorrelation functions obtained with and without the multibranch cluster update before concluding with a discussion of the directed-loop equations for the Hamiltonian with various diagonal interaction included.

A. General SSE formalism

To construct the SSE representation of a quantum mechanical expectation value at temperature $T=1/\beta$;

$$\langle A \rangle = \frac{1}{Z}\mathrm{Tr}\{A e^{-\beta H}\}, \quad Z = \mathrm{Tr}\{e^{-\beta H}\}, \tag{4}$$

the Hamiltonian is first written as a sum of elementary interactions

$$H = -\sum_t \sum_a H_{t,a}, \tag{5}$$

where in a chosen basis $\{|\alpha\rangle\}$ the operators satisfy

$$H_{t,a}|\alpha\rangle \sim |\alpha'\rangle, \tag{6}$$

where $|\alpha\rangle$ and $|\alpha'\rangle$ are both basis states. The indices t and a refer to the operator types (various kinetic and potential terms) and the lattice units over which the interactions are summed (bonds, plaquettes, etc.). A unit operator $H_{0,0} \equiv 1$ is also defined. Using the Taylor expansion of $e^{-\beta H}$ truncated at order M, the partition function can then be written as [15]

$$Z = \sum_\alpha \sum_{S_M} \frac{\beta^n (M-n)!}{M!} \left\langle \alpha \left| \prod_{i=1}^{M} H_{t_i,a_i} \right| \alpha \right\rangle, \tag{7}$$

where S_M denotes a sequence of operator indices,

$$S_M = [t_1,a_1],[t_2,a_2],\ldots,[t_M,a_M], \tag{8}$$

and n denotes the number of non-$[0,0]$ elements in S_M (i.e., the actual expansion order of the terms). The finite truncation M and the use of a fill-in operator $H_{0,0}$ are not strictly necessary [16] but simplify some aspects of the algorithm. M can be adjusted during the equilibration of the simulation, so that it always exceeds the highest power n reached, $M = An_{\max}$, where a suitable value for the factor is $A \approx 1.25$. This leads to $M \sim \beta N$, where N is the system volume, and the remaining truncation error is completely negligible. The adjustment of M has been discussed in more detail in Ref. [17].

Defining a normalized state $|\alpha(p)\rangle$ obtained by acting on $|\alpha\rangle = |\alpha(0)\rangle$ with the first p operators in the product in Eq. (7),

$$|\alpha(p)\rangle \sim \prod_{i=1}^{p} H_{t_i,a_i}|\alpha\rangle, \tag{9}$$

the requirement for a nonzero contribution to Z is the propagation periodicity $|\alpha(M)\rangle = |\alpha(0)\rangle$. This implies considerable constraints on the off-diagonal operators in the product, and clearly the vast majority of the terms are zero. In an efficient SSE method, transitions $(\alpha, S_M) \to (\alpha', S'_M)$ satisfying detailed balance should be attempted only within the subset of contributing configurations. Although the details of such sampling procedures to some extent depend on the model under study, three different classes of updates are typically used. We here summarize these in general terms, before turning to the implementation for the J-K model.

(i) The expansion order n is changed in *diagonal updates*, where a fill-in unit operator is replaced by a diagonal operator from the sum (5), and vice versa, i.e., $H_{0,0} \leftrightarrow H_{d,a}$, where the type index d corresponds to a diagonal operator in the basis used.

(ii) Off-diagonal operators cannot be added and removed one by one with the periodicity constraint $|\alpha(M)\rangle = |\alpha(0)\rangle$ maintained. Local updates involving two simultaneously replaced operators can be used for this purpose [16]. However, much more efficient cluster-type updates, which may involve a large number of operators, can also be constructed [13,18]. Here the general strategy is to find a set of operators $\{t_i, a_i\}$, such that a new valid configuration can be obtained by changing only the type indices t_i. For the J-K Hamiltonian, we will discuss two such updates, directed loops and multibranch clusters.

(iii) A third type of update is one that affects only the state $|\alpha\rangle$. This state, which is just one out of the whole cycle of propagated states $|\alpha(p)\rangle$, can change also in the updates (ii) involving off-diagonal operators. However, at high temperatures many sites will frequently have no operators acting on them. The local states at these sites will then not be affected by the off-diagonal updates. They can instead be randomly modified as they do not affect the weight. Such state updates can improve the statistics at high temperatures but are often not required for the sampling to be ergodic.

B. Plaquette operators

Turning now to the J-K model, we use the standard z-component basis

$$|\alpha\rangle = |\sigma_1^z, \ldots, \sigma_N^z\rangle, \quad \sigma_i^z = \pm 1, \tag{10}$$

where $S_i^z = (1/2)\sigma_i^z$, on lattices with $N = L_x \times L_y$ sites (or N plaquettes). Typically we consider square lattices, $L_x = L_y$, but some results for rectangular, $L_x \neq L_y$, systems have also been discussed [6]. It is convenient to express all interactions in the Hamiltonian (3) in terms of plaquette operators,

$$\begin{aligned} H_{1,a} &= CI_{ijkl}, \\ H_{2,a} &= (J/2)B_{ij}I_{kl}, \\ H_{3,a} &= (J/2)B_{jk}I_{il}, \\ H_{4,a} &= (J/2)B_{kl}I_{ij}, \\ H_{5,a} &= (J/2)B_{li}I_{jk}, \\ H_{6,a} &= KP_{ijkl}, \end{aligned} \tag{11}$$

where I_{ij} and I_{ijkl} are unit operators associated with bonds and plaquettes, respectively, and the indexing is defined in Fig. 1. Up to a constant NC, the Hamiltonian is then given by a sum (5), where the type index $t = 1, \ldots, 6$, and a is the plaquette index, $a = 1, \ldots, N$. As explained above, there is also a unit operator $H_{0,0} = 1$, which is not part of the Hamiltonian but has been introduced only as a fill-in element for augmenting the operator-index sequences of length $n < M$ in the truncated partition function Eq. (7) to M.

C. Diagonal update

Because there are no diagonal operators in the original Hamiltonian (3), the constant operators $H_{1,a}$ have been added in order to enable diagonal updates of the form $[0,0] \leftrightarrow [1,a]$ in S_M. For all elements $[t_p, a_p]$ with $t_p = 0,1$, such substitutions can be carried out sequentially for $p = 1, \ldots, M$. In the $\to$ direction, the plaquette index a is chosen randomly among $1, \ldots, N$. The Metropolis acceptance probabilities are then [17]

$$P([0,0] \to [1,a]) = \frac{NC\beta}{M-n}, \tag{12}$$

$$P([1,a] \to [0,0]) = \frac{M-n+1}{NC\beta}, \tag{13}$$

where $P > 1$ should be interpreted as probability 1. If an attempt to remove a plaquette operator, i.e., $[1,a] \to [0,0]$, is not accepted, a new plaquette index a can be generated at random. Note that for this model, where the only diagonal operators are the added constants $H_{1,a}$, it is not necessary to keep track of the propagated states during the diagonal update. In general, e.g., if a diagonal interaction is added to the Hamiltonian (3), the constant C in Eqs. (12) and (13) should

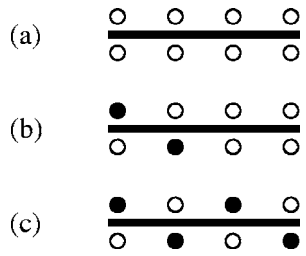

FIG. 2. Examples of vertices for the *J*-*K* model. The solid and open circles correspond to up and down spins, respectively, before (below the bar) and after (above the bar) an operator has acted. The spins on the plaquette are here drawn on a line in order to allow for a more convenient graphical representation. The order of the sites correspond to the indices i,j,k,l in Fig. 1 from left to right. (a) is one out of 16 diagonal C vertices, (b) is one out of 32 J vertices (which flip two spins), and (c) is one of the two K vertices (which flip all four spins).

be replaced by the matrix element $\langle\alpha(p)|H_{1,a_p}|\alpha(p-1)\rangle = \langle\alpha(p)|H_{1,a_p}|\alpha(p)\rangle$ of the diagonal operator in the propagated state at which the replacement is done.

D. Linked vertices

In the directed-loop and multibranch cluster updates, which we will discuss below, it is useful to represent the matrix elements in Eq. (7) as a linked lists of "vertices" [18]. The weight of a configuration (α, S_M) can be written as

$$W(\alpha,S_M) = \frac{\beta^n (M-n)!}{M!} \prod_{p=1}^{M} W(p), \tag{14}$$

where $W(p)$ is a *vertex weight*, which is simply the matrix element of the corresponding plaquette operator at position p in S_M;

$$W(p) = \langle\alpha(p)|H_{t_p,a_p}|\alpha(p-1)\rangle, \tag{15}$$

which with the operators (11) can take the value C, $J/2$, or K. Since the loop and cluster updates are carried out within sectors of fixed n (only the diagonal update changes n), the fill-in operators $H_{0,0}$ are not needed in the linked-vertex representation. A vertex represents the local four-spin states on plaquette a_p in the matrix element (15) before and after the plaquette operator has acted. These eight spin states constitute the *legs* of the vertex. For the *J*-*K* model, there are three classes of vertices, as illustrated in Fig. 2. The constant operators $H_{1,a}$ correspond to C vertices (with weight C), the bond-flip operators $H_{2,a}$–$H_{5,a}$ to J vertices (with weight $J/2$), and the plaquette-flip operators $H_{6,a}$ to K vertices (with weight K). An example of a linked-vertex representation of a term with three plaquette operators is shown in Fig. 3. The links connect vertex legs on the same site, so that from each leg of each vertex, one can reach the next or previous vertex leg on the same site (i.e., the links are bidirectional). In cases where there is only one operator acting on a given site, the corresponding "before" and "after" legs of the same vertex are linked to each other (as is the case with the legs on sites 1 and 2 in Fig. 3).

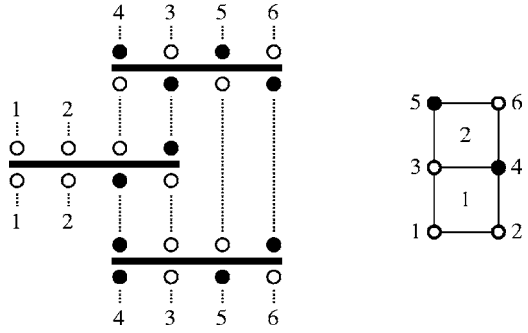

FIG. 3. The linked-vertex representation corresponding to the matrix element $\langle\alpha|H_{6,2}H_{4,1}H_{4,2}|\alpha\rangle$ (left), where the basis state $|\alpha\rangle = |\downarrow\downarrow\downarrow\uparrow\uparrow\downarrow\rangle$ (right). The bidirectional links are represented as dashed lines. The site and plaquette numbering for the six-site lattice is shown to the right. The numbers at the vertex legs indicate links across the periodic propagation boundary, and the corresponding spins are hence the same as in the state $|\alpha\rangle$. The numbers here also correspond to the site numbering of the lattice shown to the right.

During the simulation, the spin state $|\alpha\rangle$ and the operator list S_M are stored at all times. The linked-vertex representation is created after each full sweep of diagonal updates. After the directed-loop and multibranch cluster updates have been carried out, the changes are mapped back into a new $|\alpha\rangle$ and S_M. We will not discuss here how these data structures are implemented and used in practice in a computer program. The procedures are completely analogous to simulations with two-body interactions, for which an implementation was described in detail in Ref. [12].

E. Directed loops

In the original world-line QMC loop algorithm [23], spins are flipped along a one-dimensional closed path (the loop) on the space-time lattice of the discretized (Trotter decomposed) or continuous [24] path-integral representation [21]. The path is self-avoiding, and a configuration can be subdivided into loops that may be flipped independently of each other. Allowing the path to self-intersect and back-track, one can construct valid algorithms for a much larger class of models. Such general loop-type algorithms have been constructed both for continuous-time world lines (the worm algorithm [25]) and for SSE (the operator-loop algorithm [18]) [22]. The detailed balance equations—the directed-loop equations—that must be satisfied when constructing general self-intersecting and back-tracking loops were recently derived within the SSE framework, and a generalization to the path integral representation was also shown [12]. Here we will implement the directed-loop scheme for SSE sampling of the J and K terms.

In an SSE operator-loop algorithm, where the loops constitute connected strings of operators (or vertices in the linked-vertex representation) [18], the building of a loop consists of a series of steps, in each of which a vertex is entered at one leg (the entrance leg) and an exit leg is chosen according to probabilities that depend on the entrance leg and the spin states at all the legs. The entrance to the follow-

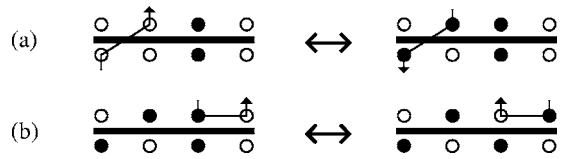

FIG. 4. Two examples of vertex paths that are related in the directed-loop scheme. (a) shows a process, and its reverse, where a C vertex is transformed into a J vertex. (b) shows two related $J \leftrightarrow K$ transformations. In the loop construction the spin states at the entrance and exit legs are flipped. The spin states shown in the vertices here are those before the flips have been carried out.

ing vertex is given by the link from the chosen exit leg. The spins at all vertex legs visited are flipped during the loop building.

The original starting point of the loop is chosen at random. Two *link discontinuities* are created when the first pair of entrance and exit spins is flipped, i.e., the legs to which these are linked will be in different spin states (this is analogous to introducing the two sources in the worm algorithm [25]). Configurations contributing to Z only contain links between legs in the same spin states. One of the discontinuities will be propagated during the loop building, whereas the other one will remain at the original starting point. The loop closes when the propagating discontinuity reaches the stationary one, so that they annihilate each other. A new contributing configuration has then been generated. If the path is self-intersecting (which is not always the case [18]), the changes in the configuration may in effect correspond to several disconnected loops.

When a vertex has been entered at a given leg, the probabilities for choosing one out of the possible exit legs have to be chosen so that detailed balance is satisfied. In general, these probabilities are not unique, and in most cases the most evident ones involve high probabilities for *bounces*, where the exit and entrance legs are the same and the loop building hence backtracks one step [18]. It is normally [26] desirable to minimize the probability of bounces. The directed-loop scheme [12] systematizes the search for valid sets of exit probabilities and enables a minimization of the bounce probability. To construct the directed-loop equations for the exit probabilities, weights are first assigned to all possible paths through a vertex from a given entrance leg. The sum of all these path weights must equal the *bare vertex weight* (15), i.e., the matrix element before the entrance and exits spins have been flipped. The actual normalized exit probability is the path weight divided by the bare vertex weight. The key element of the scheme is that weights for vertex paths that constitute each other's reverses have to be equal in order for detailed balance to be fulfilled (a generalized scheme where this is not necessarily the case has also been discussed recently [26]). Examples of such related vertex paths in the J-K model are shown in Fig. 4. The directed-loop equations written down on the basis of these simple rules often form several different closed sets that can be solved for the path weights independently of each other. Because of symmetries, many of the equation sets can be identical. In general, the directed loop equations have an infinite number of solutions, which can be significantly restricted by minimizing the

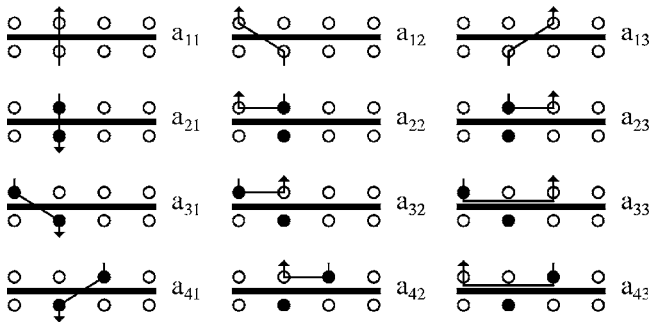

FIG. 5. A closed set of C and J vertex paths, with their corresponding weights a_{ij} that have to satisfy the directed-loop equations.

bounce probabilities. In some cases there is a unique minimum-bounce solution (sometimes with zero bounce probability), but often there is still a high degree of freedom left [12,27,28].

For the J-K model, a one-dimensional path segment can in one step transform a C vertex into a J vertex, and vice versa, an example of which is shown in Fig. 4(a). A J vertex can be transformed into a K vertex, and vice versa, as shown in Fig. 4(b). C and K vertices cannot be directly transformed into each other, however. As a consequence, the closed sets of vertex paths that contain $C \leftrightarrow J$ transformations are independent from those containing $J \leftrightarrow K$ transformations.

The closed sets containing $C \leftrightarrow J$ transformations are similar to those for the XY model [12], although the sets are larger because a C vertex can be transformed into two different J vertices. As in the XY model, no bounces are required for detailed balance in this case (until we discuss the inclusion of additional diagonal interactions in Sec. IV). One closed set with $C \leftrightarrow J$ transformations is shown in Fig. 5. To construct such a set, one first selects a "reference" vertex (any vertex) and an entrance leg, and then finds all paths that lead to new valid vertices, sampling all allowed exit legs. This corresponds to the first row of Fig. 5, where the bounce process has not been included since, as will be shown below, its weight can be set to zero in this case. Each of the resulting vertices (i.e., when the entrance and exit spins have been flipped) is then considered in turn, using as the entrance legs the exit legs from the previous step. This leads to rows two to four in Fig. 5. The procedure is repeated for each new combination of vertex and exit leg that is created. This systematically generates all pairs of vertex-paths that constitute each other's reverses, i.e., those that must have equal weights for detailed balance to be satisfied. In the case considered here, no new vertex paths are created after row four, as the reverse of each path has then already been generated. The set is hence closed. Other closed sets are constructed by picking a starting vertex and entrance leg combination that has not yet appeared within the sets already completed. This is repeated until all vertices and entrance legs combinations have been exhausted.

The directed loop equations corresponding to the closed set shown in Fig. 5 are

$$a_{11} + a_{12} + a_{13} = W_1 = C,$$

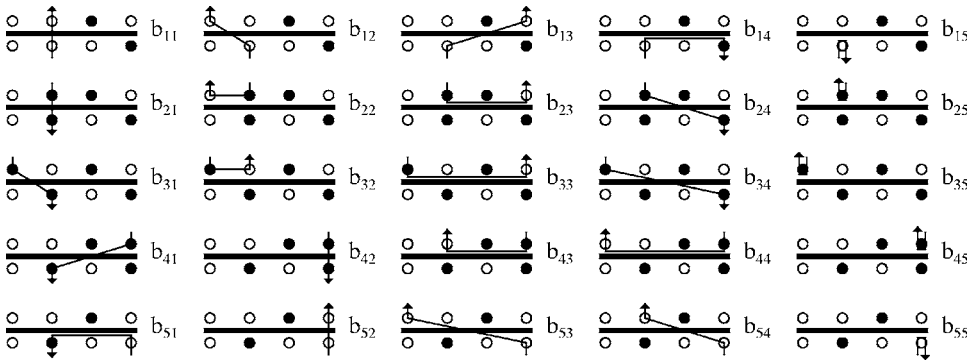

FIG. 6. A closed set of vertex paths with $J \leftrightarrow K$ transformations, labeled by their path weights b_{ij}.

$$a_{21} + a_{22} + a_{23} = W_2 = C,$$

$$a_{31} + a_{32} + a_{33} = W_3 = J/2,$$

$$a_{41} + a_{42} + a_{43} = W_4 = J/2, \tag{16}$$

where the weights a_{ij} are identified with the paths in the figure and W_i are the bare vertex weights before the entrance and exit spins have been flipped. Detailed balance requires that the weights corresponding to opposite vertex paths are equal, i.e.,

$$a_{21} = a_{11},$$

$$a_{31} = a_{12},$$

$$a_{32} = a_{22},$$

$$a_{41} = a_{13},$$

$$a_{42} = a_{23},$$

$$a_{43} = a_{33}. \tag{17}$$

The weights also have to be positive definite, since they are related to probabilities by dividing with the positive matrix elements W_i. Even with these constraints, the solution is not unique. One can reasonably assume that the most efficient solution also has equal weights for paths that are related by symmetries, e.g., $a_{12}=a_{13}$. Using all such symmetries, the solution is still not unique, however. It can be expected that it is efficient to maximize the weights of the paths that transform a C vertex into a J vertex, which is equivalent to minimizing the weights of the *continue-straight* paths that transform a C vertex into another C vertex. We have no proof of our assertion that this is a good strategy, but as it is a quite challenging task to investigate all possible valid solutions, we will use it and leave other possibilities for future studies (this issue has in fact recently been addressed in the context of other models [29]). In Fig. 5, there are only two $C \rightarrow C$ paths; the pair with weights a_{11}, a_{21}. The minimum value of these is $a_{11}=a_{21}=C-J/2$, which also implies $C \geqslant J/2$. There are now enough conditions to render a unique solution to this set of directed loop equations;

$$a_{11} = C - J/2, \quad a_{12} = J/4, \quad a_{13} = J/4,$$

$$a_{21} = C - J/2, \quad a_{22} = J/4, \quad a_{23} = J/4,$$

$$a_{31} = J/4, \quad a_{32} = J/4, \quad a_{33} = 0,$$

$$a_{41} = J/4, \quad a_{42} = J/4, \quad a_{43} = 0. \tag{18}$$

The actual exit probabilities $P^a_{ij}=a_{ij}/W_i$ are

$$P^a_{11} = 1 - J/2C, \quad P^a_{12} = J/4C, \quad P^a_{13} = J/4C,$$

$$P^a_{21} = 1 - J/2C, \quad P^a_{22} = J/4C, \quad P^a_{23} = J/4C,$$

$$P^a_{21} = 1/2, \quad P^a_{22} = 1/2, \quad P^a_{23} = 0,$$

$$P^a_{41} = 1/2, \quad P^a_{42} = 1/2, \quad P^a_{43} = 0, \tag{19}$$

where the superscript a is used as a reminder that these probabilities correspond to the paths shown in Fig. 5. Note that the probabilities here depend only on the type of vertex transformation, $C \rightarrow C(P=1-J/2C)$, $C \rightarrow J(P=J/2C)$, $J \rightarrow J(P=0)$, or $J \rightarrow C(P=1/2)$, which can aid the implementation of the probability tables in the code. All other sets with $C \leftrightarrow J$ transformations are either related by trivial symmetries to that shown in Fig. 5 or are very similar to it. The exit probabilities are given simply by the type of the corresponding vertex transformation exactly as above.

The directed-loop equations for the closed sets of paths that involve $J \leftrightarrow K$ transformations sometimes require nonzero bounce probabilities. A closed set of paths is shown in Fig. 6. The corresponding equations for the path weights b_{ij} are

$$b_{11} + b_{12} + b_{13} + b_{14} + b_{15} = J/2,$$

$$b_{21} + b_{22} + b_{23} + b_{24} + b_{25} = J/2,$$

$$b_{31} + b_{32} + b_{33} + b_{34} + b_{35} = K,$$

$$b_{41} + b_{42} + b_{43} + b_{44} + b_{45} = J/2,$$

$$b_{51} + b_{52} + b_{53} + b_{54} + b_{55} = J/2. \tag{20}$$

Again, we will assume that it is advantageous to minimize the bounce probabilities, i.e., the bounce weights $b_{i,5}$ above. For $K \leqslant 2J$ all the bounce weights can in fact be zero. The weight of the continue-straight paths (e.g., b_{11}), which here

transform a J vertex into a J vertex with the same spin flips (i.e., the same plaquette operator), can be set to zero. A symmetric $K \leqslant 2J$ solution is then

$$b_{11}=0, \quad b_{12}=K/4, \quad b_{13}=J/4-K/8,$$

$$b_{14}=J/4-K/8, \quad b_{15}=0,$$

$$b_{21}=0, \quad b_{22}=K/4, \quad b_{23}=J/4-K/8,$$

$$b_{24}=J/4-K/8, \quad b_{25}=0,$$

$$b_{31}=K/4, \quad b_{32}=K/4, \quad b_{33}=K/4, \quad b_{34}=K/4, \quad b_{35}=0,$$

$$b_{41}=J/4-K/8, \quad b_{42}=0, \quad b_{43}=J/4-K/8,$$

$$b_{44}=K/4, \quad b_{45}=0,$$

$$b_{51}=J/4-K/8, \quad b_{52}=0, \quad b_{53}=K/4, \quad b_{54}=J/4-K/8,$$

$$b_{55}=0. \tag{21}$$

For $K>2J$, the bounce weight b_{35} has to be nonzero for a positive definite solution. Minimizing this weight one obtains the following solution:

$$b_{11}=0, \quad b_{12}=J/2, \quad b_{13}=0, \quad b_{14}=0, \quad b_{15}=0,$$

$$b_{21}=0, \quad b_{22}=J/2, \quad b_{23}=0, \quad b_{24}=0, \quad b_{25}=0,$$

$$b_{31}=J/2, \quad b_{32}=J/2, \quad b_{33}=J/2, \quad b_{34}=J/2, \quad b_{35}=K-2J,$$

$$b_{41}=0, \quad b_{42}=0, \quad b_{43}=0, \quad b_{44}=J/2, \quad b_{45}=0,$$

$$b_{51}=0, \quad b_{52}=0, \quad b_{53}=J/2, \quad b_{54}=0, \quad b_{55}=0. \tag{22}$$

The exit probabilities are hence, for $K \leqslant 2J$,

$$p^b_{11}=0, \quad P^b_{12}=K/2J, \quad P^b_{13}=1/2-K/4J,$$

$$P^b_{14}=1/2-K/4J, \quad P^b_{15}=0,$$

$$p^b_{21}=0, \quad P^b_{22}=K/2J, \quad P^b_{23}=1/2-K/4J,$$

$$P^b_{24}=1/2-K/4J, \quad P^b_{25}=0,$$

$$p^b_{31}=1/4, \quad P^b_{32}=1/4, \quad P^b_{33}=1/4, \quad P^b_{34}=1/4, \quad P^b_{35}=0,$$

$$p^b_{41}=1/2-K/4J, \quad P^b_{42}=0,$$

$$P^b_{43}=1/2-K/4J, \quad P^b_{44}=K/2J, \quad P^b_{45}=0,$$

$$p^b_{51}=1/2-K/4J, \quad P^b_{52}=0, \quad P^b_{53}=K/2J,$$

$$P^b_{54}=1/2-K/4J, \quad P^b_{55}=0, \tag{23}$$

and for $K>2J$

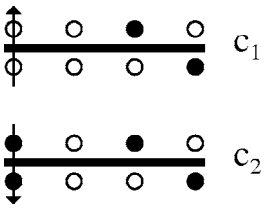

FIG. 7. A closed set of two vertex paths, where only the continue-straight process is allowed and a J vertex is transformed into another J vertex with probability 1.

$$P^b_{11}=0, \quad P^b_{12}=1, \quad P^b_{13}=0, \quad P^b_{14}=0, \quad P^b_{15}=0,$$

$$P^b_{21}=0, \quad P^b_{22}=1, \quad P^b_{23}=0, \quad P^b_{24}=0, \quad P^b_{25}=0,$$

$$P^b_{31}=J/2K, \quad P^b_{32}=J/2K, \quad P^b_{33}=J/2K, \quad P^b_{34}=J/2K,$$

$$P^b_{35}=1-2J/K,$$

$$P^b_{41}=0, \quad P^b_{42}=0, \quad P^b_{43}=0, \quad P^b_{44}=1, \quad P^b_{45}=0,$$

$$P^b_{51}=0, \quad P^b_{52}=0, \quad P^b_{53}=1, \quad P^b_{54}=0, \quad P^b_{55}=0. \tag{24}$$

Note that the solution is continuous across $K=2J$.

Also in this case the probabilities are seen to depend only on the type of vertex class transformation, $J \to J$, $J \to J'$, $J \to K$, $K \to J$, or $K \to K$ (bounce). Here one has to distinguish between a continue-straight $J \to J$ transformation where the spin flip remains on the same bond (e.g., b_{11}), and a $J \to J'$ transformations where the spin flip moves to a neighboring bond on the plaquette (e.g., b_{13}).

There is one more type of closed set of vertex paths, an example of which is shown in Fig. 7. In this case, neither a valid K vertex nor a J vertex with the flip moved to a different nearest-neighbor pair can be reached from the J vertex and the chosen entrance leg. As the two vertices shown have the same bare weights, no bounce processes have to be included and the exit is unique:

$$P^c_1=1,$$

$$P^c_2=1. \tag{25}$$

All closed sets of vertex paths can be related to those shown in Figs. 5–7, and in all cases the probabilities depend only on how the paths transform the vertices between the classes C, J, and K. This simplifying property will be discussed further in Sec. IV, where we consider inclusions of additional diagonal interactions in the Hamiltonian. In that case the solutions to the equations become more complicated; however, the directed-loop framework is still required in order to develop efficient codes. For the case of zero diagonal interactions, Eq. (3), the exit probabilities for the J-K model are summarized in Table I.

To carry out a directed-loop update, a vertex leg is first chosen at random. This entrance leg together with all the spin states on the vertex determine which one of the exit probabilities in Table I should be applied when generating the exit leg. These probabilities are stored in a pregenerated

TABLE I. All exit probabilities for the J-K model. The initial vertex class is indicated in front of the square brackets, and the new class after the arrow. All the possible vertex classes that can be generated from a given vertex and entrance leg are listed within the square brackets. In cases where more than one vertex of a given class can be generated, the corresponding symbol appears multiple times. J, J', and J'' denote subclasses of J vertices in which different spin pairs are flipped. The sets a, b, and c correspond to Figs. 5–7; all other sets are related to these by symmetries. The only bounce process is $K \to K$; all $C \to C$ and $J \to J$ cases correspond to continue-straight paths.

Vertex transformation	Set	$P(K \leqslant 2J)$	$P(K > 2J)$
C-$[C,J,J'] \to C$	a	$1-J/2C$	$1-J/2C$
C-$[C,J,J'] \to J,J'$	a	$J/4C$	$J/4C$
J-$[C,C,J'] \to C,C$	a	$1/2$	$1/2$
J-$[C,C,J'] \to J'$	a	0	0
J-$[J,J',J'',K] \to J$	b	0	0
J-$[J,J',J'',K] \to J',J''$	b	$1/2-K/4J$	0
J-$[J,J',J'',K] \to K$	b	$K/2J$	1
K-$[J,J,J',J',K] \to J,J,J',J'$	b	$1/4$	$J/2K$
K-$[J,J,J',J',K] \to K$	b	0	$1-2J/K$
J-$[J] \to J$	c	1	1

table. When the exit has been selected, the link from it is used to enter another vertex, from which an exit is again chosen, etc., until the loop closes. The number of loops to be generated during each Monte Carlo step is adjusted such that the total number of vertices visited is, on average, of the same order as (e.g., equal to or twice) the number of vertex legs ($8n$), e.g., $4\langle n \rangle$ or $4M$.

In some cases, a loop can become very long before it closes. In order to avoid problems with loops that do not close within a reasonable time, one can impose a maximum loop length. If this limit is exceeded, the loop building is terminated and the changes in the vertices are disregarded. This does not introduce any bias in quantities measured in the (α, S_M) representation, since if an update is is precluded by this prescription the reverse update is also precluded, and hence detailed balance in the (α, S_M) space is not affected. Loop termination would affect measurements of the single-particle Green's function, which is done in the space of incomplete loops [25,30]. In practice, the termination can easily be accomplished by simply exiting the loop-update routine without mapping the linked-vertex representation back into a state $|\alpha\rangle$ and an operator list S_M; in order to discard only the loop currently under construction, its history would have to be stored. Hence, not only the terminated loop itself is discarded, but also all other loops constructed since the previous diagonal update. This is not a problem as long as termination does not occur frequently. We typically set the maximum loop length to $\approx 100\langle n \rangle$, and the fraction of terminated loops is then very small.

F. Multibranch clusters

Since a K vertex cannot be generated directly out of a C vertex, but requires the presence of J vertices, the directed-loop update cannot be used when $J=0$. As will be demonstrated in Sec. III, this update is also inefficient for large K/J. This can be understood from Table I, where the bounce probability off a K vertex is seen to approach 1 as $K \to \infty$. In principle the directed-loop update, in combination with the diagonal update, is ergodic for any finite K/J, but for $K/J \gtrsim 14$ (in the CDW phase) it becomes difficult to obtain good results this way. In order to improve the performance for large K/J, a type of multibranch cluster update is developed here. It is similar to a quantum cluster update recently developed for the transverse Ising model [13], where it can be considered a direct generalization of the classical Swendsen-Wang algorithm [31]. The multibranch cluster update for the J-K model is more complex, due to the larger number of different interaction vertices and the multitude of possible transformations among them.

In order to transform a C vertex directly into a K vertex, spins at four legs have to be flipped. If this is done, spins also have to be flipped at all the legs to which these four legs are linked. This will in turn force additional spin flips in the vertices to which they are linked, etc. Clearly, such a process can branch out very quickly to a large number of vertices. Even if a scheme can be found where detailed balance is maintained, there is in general nothing that guarantees that the process ever terminates (i.e., the cluster may not complete). For the J-K model, this proliferation problem can be solved by defining a unique set of exit legs, given an entrance leg and all the eight spin states of the vertex. If the constant C is chosen equal to K, which with the directed loop probabilities in Table I can be done if $K \geqslant J/2$, $C \leftrightarrow K$ transformations will lead to no weight changes. If J vertices are always transformed into other J vertices, there are also no weight changes in these processes. A single constructed cluster can therefore be flipped with probability 1, corresponding to a Wolff-type update [22]. One can also subdivide the whole linked vertex list into clusters that can be flipped independently of each other with probability $1/2$. This Swendsen-Wang-type approach will be used here.

Figure 8 shows the branching rules for all different types of vertices. The cases (d) and (e) correspond to $C \leftrightarrow K$ transformations. In all other cases the vertex class does not change, but note that J vertices are transformed into J vertices with a different pair of flipped spins (i.e., the corresponding plaquette operator changes). The outgoing arrows point to entrances to other vertices, to which the same branching rules are applied. However, if an exit leg is linked to a leg that has already been visited, this leg should not be visited again. In terms of the graphical representation used in Fig. 8, a vertex leg should not be entered if it already has an outgoing arrow. If a vertex is entered for a second time, and hence has arrows at four legs (those with eight exit legs in Fig. 8 can clearly only be visited once), the second set of exit legs are exactly the four that were not previously assigned arrows. In other words, all vertices in (c)–(i) can be assigned outgoing arrows in two different ways, and the set chosen is the one to which the entrance leg belongs. Furthermore, the two sets of mutually exclusive exit legs are exactly the same in the vertices obtained when the legs in one of these sets are flipped. This solves the proliferation problem, since it is guaranteed that a vertex leg can be visited only once. It also allows for independent flips of all clusters.

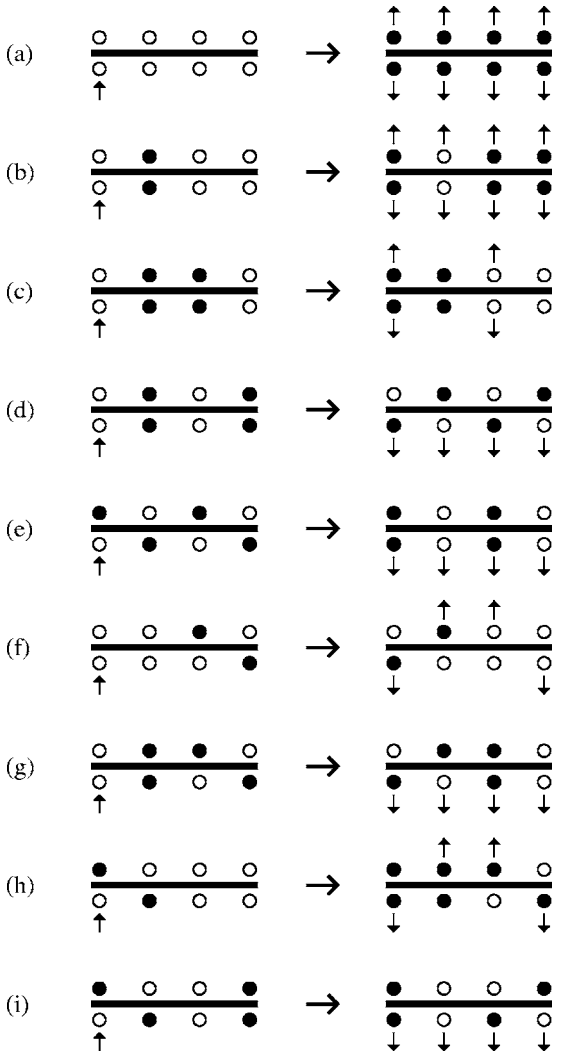

FIG. 8. Vertex transformations in the multibranch cluster update. The entrance leg is denoted by an arrow pointing into the vertices on the left. In the updated vertices to the right, the spins at the outgoing arrows have been flipped. The branching for all entrance legs and vertices not shown here are obtained by applying trivial symmetries to one of the cases shown in (a)–(i).

To start a cluster, a vertex leg which does not belong to a cluster already constructed is first chosen at random, and the branching is assigned according to the rules defined in Fig. 8. Flags are set on all the exit legs, to indicate that they have been visited (corresponding to the outgoing arrows Fig. 8). Note that the entrance also becomes an exit leg with an outgoing arrow. If the cluster is to be flipped (which it should be with probability 1/2), the spins at all the exit legs are flipped. All exit legs are put on a stack. They are subsequently picked one by one from the stack, and the legs to which they are linked are used as entrance legs to other vertices if they have not yet been visited, i.e., these legs are flipped and put on the stack only if they have not been visited before. In the graphical representation, a cluster branch ends when an arrow is encountered. The whole cluster is completed when all arrows point to other arrows; the stack with unprocessed entrance legs is then empty. A completed cluster with only two vertices is illustrated in Fig. 9.

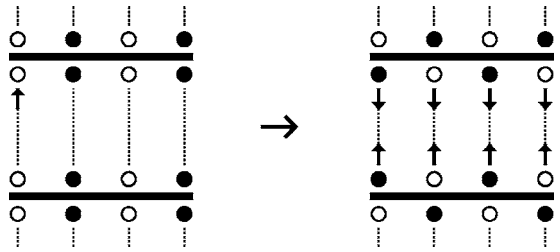

FIG. 9. Multibranch cluster update in which two C vertices are transformed into two K vertices. The initial entrance leg is at the inward pointing arrow in the linked-vertex representation to the left. The resulting vertices with their arrows indicating legs visited are shown to the right.

Although the autocorrelation measurements discussed in Sec. III provide a quantification of the effectiveness of the multibranch cluster updates, we pause here to simply illustrate the cluster characteristics as implemented for our J-K model. A histogram of cluster sizes generated at large K/J is shown in Fig. 10. Clearly, the vast majority of clusters built in this case are small eight-leg clusters (an example of which is illustrated in Fig. 9), with significant occupation in the smaller bins up to clusters of size 128. A second peak occurs in the histogram at much larger sizes, around 90% of the total number of vertex legs. This distribution of cluster sizes reflects the fact that every configuration contains one big cluster, and a large number of small clusters. The large clus-

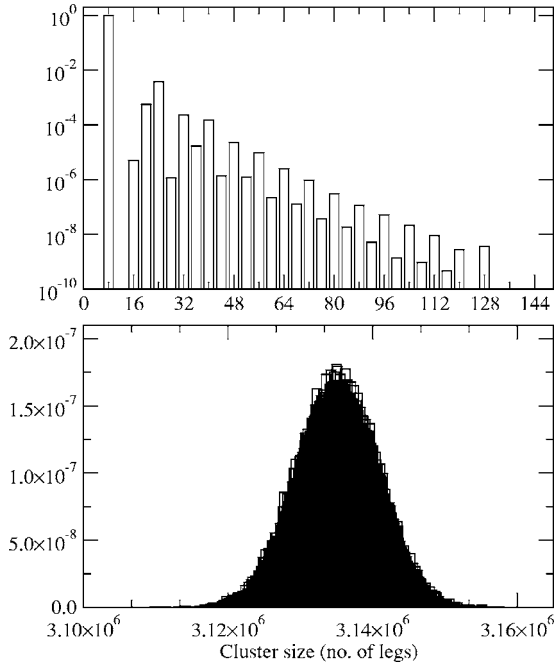

FIG. 10. Probability histogram of cluster sizes (measured as the number of vertex legs in a cluster) produced by multibranch cluster updates on a 16×16 lattice at $K/J=80$ and $\beta=32$. The average length of the operator list for this simulation was $\langle n\rangle\approx4.35\times10^{5}$ (i.e., approximately 3.5×10^{6} vertex legs). Data in the upper figure are for the smaller bins, while data in the lower figure were rebinned to 100 legs per bin. All intermediate occupations were measured as zero.

ter spans about 90% of the vertex legs, almost independently of the value of K/J. Hence the cluster size distribution is by no means optimal, in the sense that the typical cluster size does not reflect a physical correlation length of the system. In any case the multibranch update significantly improves the performance for large K/J, as will be shown in Sec. III. This can probably partially be explained by the fact that the directed-loop updates become very inefficient as $K/J \to \infty$, and hence the multibranch clusters can help performance significantly, even though the cluster-size distribution is not necessary optimal.

G. Physical observables

In this section we summarize the physical observables relevant to studies of the J-K model [5–7,11], and present the estimators used to evaluate them in the SSE method. The general forms of the estimators have been derived in previous papers [15–17,32]; here we only apply those derived forms to the particular quantities of interest for the J-K model.

We typically carry out measurements on the configurations generated after every Monte Carlo step (MCS), with a MCS defined as a sweep of diagonal updates, followed by construction of the linked-vertex list, in which a fixed number of loop updates are carried out. In the same linked list, all multibranch clusters are constructed and flipped with probability 1/2. After this, the updated vertex list is mapped back into a new state $|\alpha\rangle$ and an operator list S_M. This is the representation used for the measurements. The fill-in elements $H_{0,0}$ in S_M are irrelevant at this stage, and we therefore now consider the reduced list S_n without these operators. There are hence $n+1$ propagated states $|\alpha(p)\rangle = |\sigma_1^z(p), \ldots, \sigma_N^z(p)\rangle$, which are obtained one by one when operating with the first p operators, $p=0, \ldots, n$, on the initially stored state $|\alpha(0)\rangle = |\alpha(n)\rangle$. Although measurements can involve all the states, at any given time only a single $|\alpha(p)\rangle$ has to be stored.

The z component of the spin-spin correlation function can be easily obtained, as it is diagonal in the representation used. Equal-time correlations can be averaged over the propagated states, i.e.,

$$\langle S_k^z S_l^z \rangle = \frac{1}{4} \left\langle \frac{1}{n} \sum_{p=0}^{n-1} \sigma_k^z(p) \sigma_l^z(p) \right\rangle, \tag{26}$$

where in the special case $n=0$, which occurs in practice only for small N at very high temperatures, the averaged sum should be replaced by $\sigma_k^z(0)\sigma_l^z(0)$. Since states p and $p+1$ differ only by two or four flipped spins, the sum in Eq. (26) can be replaced by a sum where only, e.g., every Nth state is included. We often consider the Fourier transform of the correlation function, i.e., the static spin structure factor

$$S_s(q_x, q_y) = \frac{1}{N} \sum_{k,l} e^{i(\mathbf{r}_k - \mathbf{r}_l)\cdot \mathbf{q}} \langle S_k^z S_l^z \rangle, \tag{27}$$

where $r_i = (x_i, y_i)$ is the lattice coordinate (with lattice spacing 1) and $q = (q_x, q_y)$ is the wave vector. We also study the corresponding static susceptibility,

$$\chi_s(q_x, q_y) = \frac{1}{N} \sum_{k,l} e^{i(\mathbf{r}_k - \mathbf{r}_l)\cdot \mathbf{q}} \int_0^\beta \langle S_k^z(\tau) S_l^z(0) \rangle. \tag{28}$$

It has been shown [15] that the SSE estimator for the Kubo integral is

$$\int_0^\beta d\tau \langle S_k^z(\tau) S_l^z(0) \rangle = \frac{\beta}{4} \left\langle \frac{1}{n(n+1)} \left[\left(\sum_{p=0}^{n-1} \sigma_k^z(p) \right) \left(\sum_{p=0}^{n-1} \sigma_l^z(p) \right) + \sum_{p=0}^{n-1} \sigma_k^z(p) \sigma_l^z(p) \right] \right\rangle. \tag{29}$$

Here the first term typically dominates; it is obtained by first summing the spins at k and l over the propagated states, and then multiplying the sums. The full sums must clearly be calculated here, but one can still take advantage of the fact that only two or four out of the N spins $\sigma_k^z(p)$ change at every propagation $p \to p+1$. One can thus evaluate the sums for all sites k in $\sim n \sim N\beta$ steps. The second term in Eq. (29) vanishes as $N \to \infty$, but typically it gives a non-negligible relative contribution for small-N calculations and should always be kept. This sum is the same as in the equal-time correlation (26) and can again be replaced by a partial summation without introducing a bias. In the case $n=0$, the whole expression within $\langle\ \rangle$ in Eq. (29) should be replaced by $\sigma_k^z(0)\sigma_l^z(p)$.

We are also interested in the spin stiffness, or the superfluid density in the boson representation, which at finite temperature is defined by

$$\rho_s = \frac{1}{N} \frac{\partial^2 F(\phi)}{\partial \phi^2} = \lim_{\phi \to 0} \frac{\Delta F}{N} \frac{2}{\phi^2}, \tag{30}$$

where F is the free energy, ϕ is an infinitesimal twist that is imposed on all bonds (i,j) in either the x or y lattice direction, and $\Delta F = F(\phi) - F(\phi=0)$. The corresponding bond operators (1) become

$$B_{ij}(\phi) = S_i^+ S_j^- (e^{i\phi}) + S_i^- S_j^+ (e^{-i\phi}). \tag{31}$$

The resulting phase factors lead to a shift in the free energy F to second order in ϕ. However, with the plaquette operator $P_{ijkl}(\phi)$, the analogous phase factors cancel, and hence it does not appear in the estimator for the stiffness. The derivative as $\phi \to 0$ in Eq. (30) can therefore be directly estimated using the winding number fluctuations in the SSE simulations, [17] in a way very similar to that done in path integral methods [33]. We define the winding numbers w_x and w_y as

$$w_\alpha = (N_\alpha^+ - N_\alpha^-)/L, \tag{32}$$

where $N_\alpha^\pm$ denote the number of operators in S_n which transport a boson (or spin $\uparrow$) ± 1 lattice steps in the α direction. In the J-K model, only the bond operators B_{ij} can transfer a net number of particles; in terms of the corresponding plaquette operators (11), the pairs $H_{2,a}$, $H_{4,a}$ and $H_{3,a}$, $H_{5,a}$ transfer particles along the x and y axis, respectively. By operating successively with all operators in S_n on the state $|\alpha\rangle$ one can determine all the numbers $N_\alpha^\pm$ needed to obtain the winding numbers. The partition function is then given by

$$Z(\phi) = \mathrm{Tr}\left\{ \sum_n \frac{(-\beta)^n}{n!} H^n e^{i\phi L w_\alpha} \right\}. \quad (33)$$

We can use the statistical mechanical definition of the free energy to calculate the difference,

$$\Delta F = -\frac{1}{\beta} \ln\left(\frac{Z(\phi)}{Z} \right) = -\frac{1}{\beta} \ln(\langle e^{i\phi L w_\alpha} \rangle). \quad (34)$$

Expanding the right-hand side and using Eq. (30), we get

$$\rho_s = \frac{1}{\beta} \langle w_\alpha^2 \rangle, \quad (35)$$

where for square system sizes we typically average over $\alpha = x, y$. This result can also be derived using spin current correlation functions [34].

In order to detect the modulations of the bond and plaquette expectation values $\langle B_{ij} \rangle$ and $\langle P_{ijkl} \rangle$ in the striped phase, one can use open boundary conditions in order to break the translational symmetry. In order to break the 90° rotational symmetry, rectangular lattices can be used. On these lattices one can observe a unique bond or plaquette pattern. [6] However, for careful finite-size scaling studies it is preferable to consider periodic $L \times L$ lattices, on which all bond and plaquette expectations average to uniform values. We hence instead consider the corresponding correlation functions, and also calculate the associated susceptibilities. The static plaquette structure factor is defined as

$$S_p(q_x, q_y) = \frac{1}{N} \sum_{a,b} e^{i(\mathbf{r}_a - \mathbf{r}_b)\cdot\mathbf{q}} \langle P_a P_b \rangle, \quad (36)$$

where P_a is the plaquette operator (2) with the plaquette subscript a defined in Fig. 1. The corresponding susceptibility is completely analogous to Eq. (28),

$$\chi_p(q_x, q_y) = \frac{1}{N} \sum_{a,b} e^{i(\mathbf{r}_a - \mathbf{r}_b)\cdot\mathbf{q}} \int_0^\beta d\tau \langle P_a(\tau) P_b(0) \rangle. \quad (37)$$

Bond structure factors and susceptibilities are defined in the same way; we here consider those corresponding to correlations between bonds in the same lattice direction. Hence, defining x_k and y_k as the nearest-neighbor sites of site k in the x and y directions, the bond structure factors $S_{b,x}$ and $S_{b,y}$ are

$$S_{b,\alpha}(q_x, q_y) = \frac{1}{N} \sum_{k,l} e^{i(\mathbf{r}_k - \mathbf{r}_l)\cdot\mathbf{q}} \langle B_{k,\alpha_k} B_{l,\alpha_l} \rangle. \quad (38)$$

The corresponding susceptibilities are again defined as in Eq. (37).

For expectation values involving products of operators that also appear as terms in the Hamiltonian, such as the above plaquette and bond structure factors and susceptibilities, the SSE estimators are remarkably simple expressions involving only numbers of operators or operator combinations in the list S_n [16]. The simplest case is the expectation value of a single operator,

$$\langle H_{t,a} \rangle = \frac{\langle n([a,b]) \rangle}{\beta}, \quad (39)$$

where $n([a,b])$ is the number of elements $[a,b]$ in the list S_n. This gives the internal energy

$$E = -\frac{\langle n \rangle}{\beta}, \quad (40)$$

which is identical to the expression obtained by Handscomb [19]. An equal-time correlation function of two operators appearing in the Hamiltonian is given by [16]

$$\langle H_{s,a} H_{t,b} \rangle = \frac{1}{\beta^2} \langle (n-1) N([s,a][t,b]) \rangle, \quad (41)$$

where $N([s,a][t,b])$ denotes the number of occurrences of the operators $[s,a]$ and $[t,b]$ next to each other, in the given order, in S_n (with the periodicity of S_n taken into account). The corresponding Kubo integral is [16]

$$\int_0^\beta d\tau \langle H_{s,a}(\tau) H_{t,b}(0) \rangle = \frac{1}{\beta} \langle N([s,a]) N([t,b]) - \delta_{st}\delta_{ab} N([s,a]) \rangle, \quad (42)$$

where $N([s,a])$ is the number of operators $[s,a]$. Using Eqs. (41) and (43), the estimators for Eqs. (36)–(38) can be easily obtained.

III. AUTOCORRELATIONS

We show here some results illustrating the performance of the algorithm, focusing in particular on the efficiency boost achieved with the multibranch update. Although we will attempt to extract the dynamic exponent of the simulations at the superfluid-VBS transition, we focus first on the simulation dynamics inside the ordered phases. Particularly in the VBS (striped) and staggered phases, which break spatial symmetries, we expect slow modes corresponding to transitions between the different degenerate states. One might also expect potential problems related to long-lived defects forming in these states.

For a quantity Q, the normalized autocorrelation function is defined in the standard way as

$$A[Q](t) = \frac{\langle Q(i+t) Q(i) \rangle - \langle Q(i) \rangle^2}{\langle Q(i)^2 \rangle} \quad (43)$$

where the averages are over the Monte Carlo time (steps) i. We will compare autocorrelation functions in the three different ordered phases, obtained in simulations with and without multibranch cluster updates. A Monte Carlo step is defined as a full sweep of diagonal updates, followed by a number of directed-loop updates, and, if multibranch updates are carried out, decomposition of the configuration into clusters, each of which is flipped with probability 1/2. In these simulations the number of directed-loop updates per step was chosen so that, on average, the total number of vertices visited is $4M$, with the truncation M of the index sequence

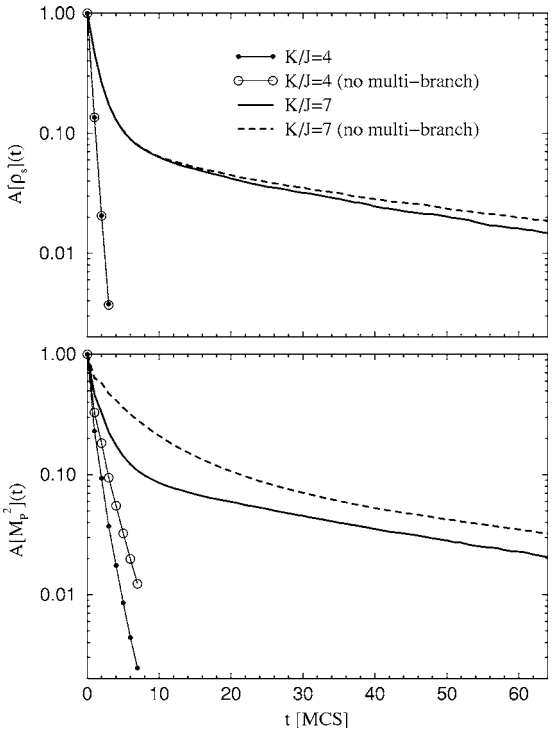

FIG. 11. Autocorrelation function for the spin stiffness (upper panel) and the plaquette-stripe order parameter (lower panel) in simulations of $L=16$ systems at $K/J=4$ and 7, both at inverse temperature $K/T=16$. Results of simulations both with and without the multibranch cluster update are shown.

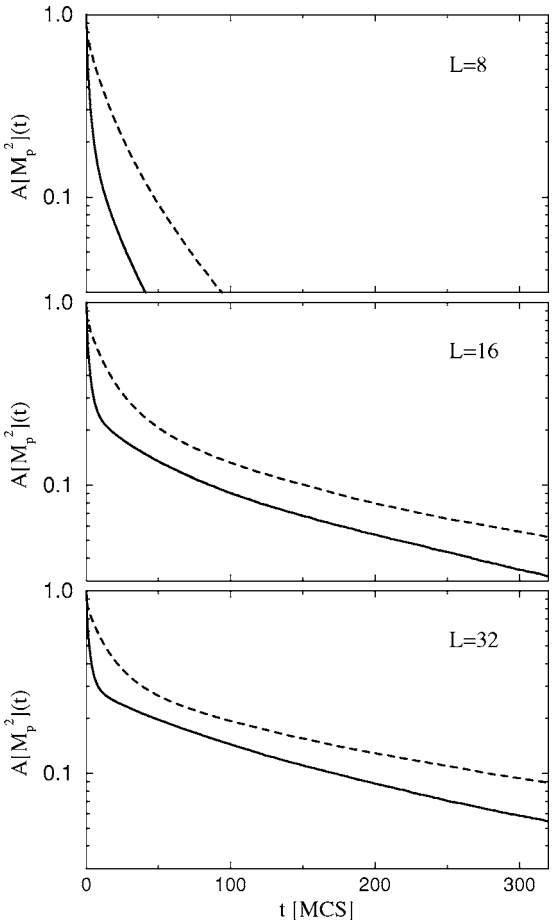

FIG. 12. Autocorrelation function for the plaquette-stripe order parameter at $K/J=12$ and inverse temperature $K/T=32$. Results with (solid curves) and without (dashed curves) multibranch clusters are compared for three different system sizes.

chosen equal to 1.25 times the maximum expansion order n reached during equilibration (the dependence of M on the length of the equilibration is in practice very small and introduces only a negligible ambiguity in the definition of the Monte Carlo time).

Figure 11 shows autocorrelation results for the superfluid density ρ_s and the squared stripe order parameter M_P^2 inside the superfluid phase for a 16×16 lattice at $K/T=16$. At $K/J=4$, the ρ_s autocorrelations drop very rapidly (the integrated autocorrelation time is less than 1), and there are no discernible effects of including multibranch updates. The autocorrelation time for M_P^2 is also very short, but here there are clear improvements with the multibranch updates. However, considering that the CPU time is almost doubled when including multibranch updates, including them at $K/J=4$ is not advantageous. At $K/J=7$, which is approaching the transition point to the striped phase at $K/J\approx7.9$, the autocorrelations decay much more slowly, and although there are visible favorable effects of the multibranch updates in both quantities, the gain is hardly worth the additional CPU time cost. In Fig. 12, results are shown for the stripe order parameter at $K/J=12$, well inside the striped phase, for three different system sizes at inverse temperature $K/T=32$. The multibranch updates have clear favorable effects on the autocorrelations, but although the initial drop is considerably faster, the asymptotic autocorrelation time, i.e., the long-time linear decay seen on the linear-log scale used in the figures, changes very little. In this case the reduction of the integrated autocorrelation time may (depending on the exact value of K/J, and the system size) motivate the additional computational effort of the multibranch update.

The multibranch cluster update improves the simulation efficiency considerably inside the CDW phase, as illustrated in Fig. 13 for three different system sizes with $K/J=32$ at a low temperature. Here the improvement in the simulation efficiency for the squared staggered order parameter M_S^2 is clearly significant enough to motivate the cost of the multibranch clusters, especially for large system sizes. An interesting feature to note here is that when the multi-branch clusters are included, the asymptotic autocorrelation time actually decreases for $L=32$ relative to $L=16$, and $L=16$ and $L=8$ show almost identical autocorrelation functions. This surprising trend for increasing L can probably be traced to the fluctuations in the CDW order parameter for a given SSE configuration. Figure 14 shows the dependence of the staggered order parameter on the propagation number p [referring to the propagated states, Eq. (9)] divided by the total number of operators n for an equilibrated configuration. The fraction p/n corresponds roughly to the normalized imaginary-time τ/β in the standard Euclidean path integral formalism [32]. For a small system, exemplified by $L=8$ in the figure, the order parameter fluctuates between positive and negative values, whereas for a large system, exemplified

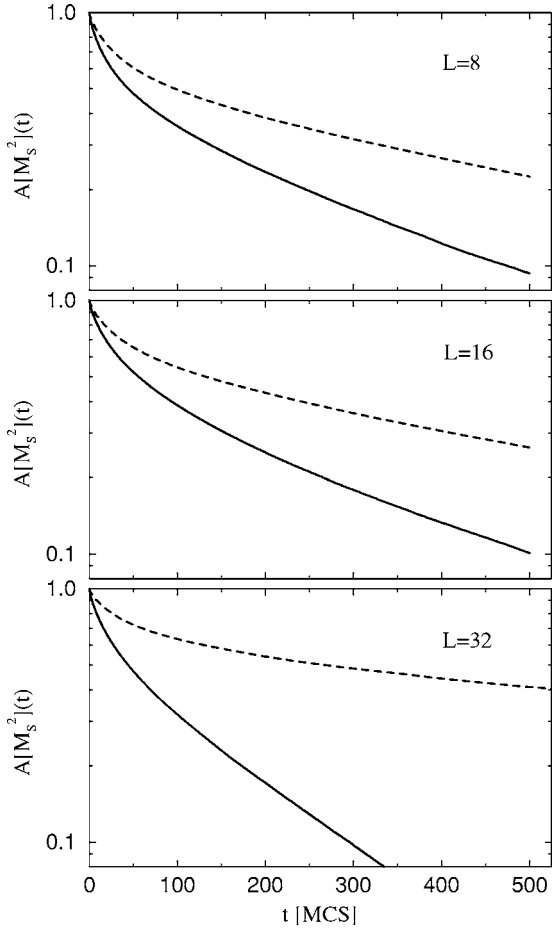

FIG. 13. Autocorrelation function for the staggered order parameter at $K/J=32$ and inverse temperature $K/T=32$. Results with (solid curves) and without (dashed curves) multibranch clusters are compared for three different system sizes.

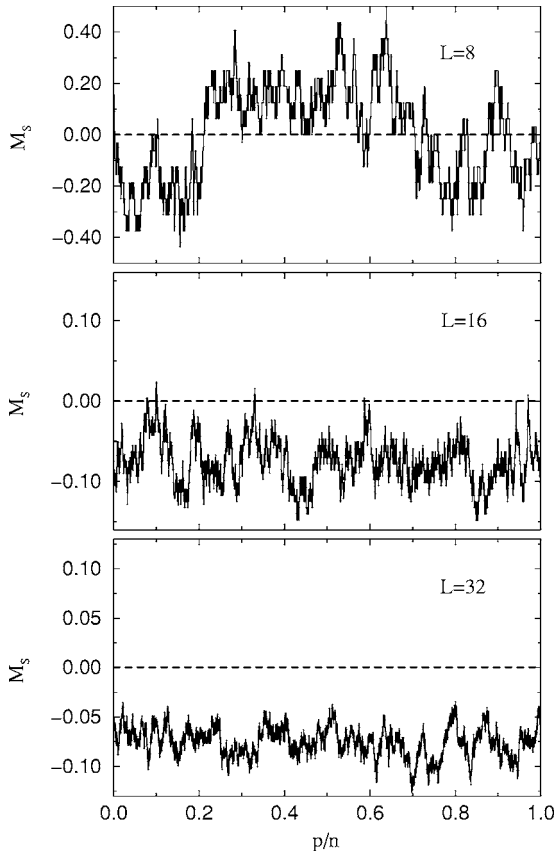

FIG. 14. The staggered magnetization vs the propagation index p (divided by the total number of operators n) in configurations generated for system sizes $L=8,16$, and 32, at $K/J=32$, $K/T=32$.

here by $L=32$, fluctuations sufficiently large to "tunnel" the system between positive and negative order parameters are very rare. Clearly, as $T\rightarrow 0$, there would be such tunneling (instanton) events also in a large system, but if T is not low compared to the gap between the symmetric and antisymmetric linear combinations of the two different real-space ordered states (which decreases exponentially fast with increasing L), such events are not present in typical configurations. The shorter autocorrelation time for $L=32$ than for $L=16$ (when multibranch updates are included) in Fig. 13 may hence be related to the larger fluctuations in M_S for the smaller system size, which can lead to instantons events that are not so easily added or removed from the configurations. For the larger system size, there are in practice no instanton at the temperature used here, and the difficulties in adding or removing them in this case would only show up at very long times as an undetectable tail in the autocorrelation function. The order parameter fluctuations are further illustrated in the form of histograms in Fig. 15 (only showing the positive part of the distributions). Here it can be seen that some instantons are still expected at $L=16$, since the probability of a zero order parameter is not negligible, but at $L=32$ the probability at zero is exponentially small and hardly any instantons would be expected on the time scale of a typical simulation.

As can be seen in Fig. 11, the asymptotic autocorrelation time for the stripe (VBS) order is quite long, approximately 40 Monte Carlo steps, in the superfluid phase at $K/J=7$ even for the modest system size $L=16$. Critical slowing down is expected as the critical superfluid-VBS point is approached, if indeed this transition is continuous (which is not presently clear). In Fig. 16 we show results for the Monte Carlo time evolution of some relevant quantities very close to the quantum phase transition. Here the lattice size $L=96$ and the temperature is chosen sufficiently low for obtaining ground state expectation values within statistical error. The points shown are averages over "bins" of 10^4 Monte Carlo steps, and clearly these bin averages are not yet statistically independent; the autocorrelation times are several 10^4 Monte Carlo steps. These simulations did include multi-branch cluster updates. Currently, high-precision $T\rightarrow 0$ converged simulations of this model close to the superfluid-VBS transition are not feasible for L much larger than 100. Note the clear anticorrelations between the stripe order and superfluid density in Fig. 16. These do not, however, give an indication of the order of the phase transition between the two phases, as anticorrelations are expected at both continuous and first-order transitions.

Finally, we discuss attempts to extract the dynamical scaling exponent z' characterizing the critical slowing down of the simulation at the superfluid-VBS phase transition. This task is complicated by the fact that we do not know with

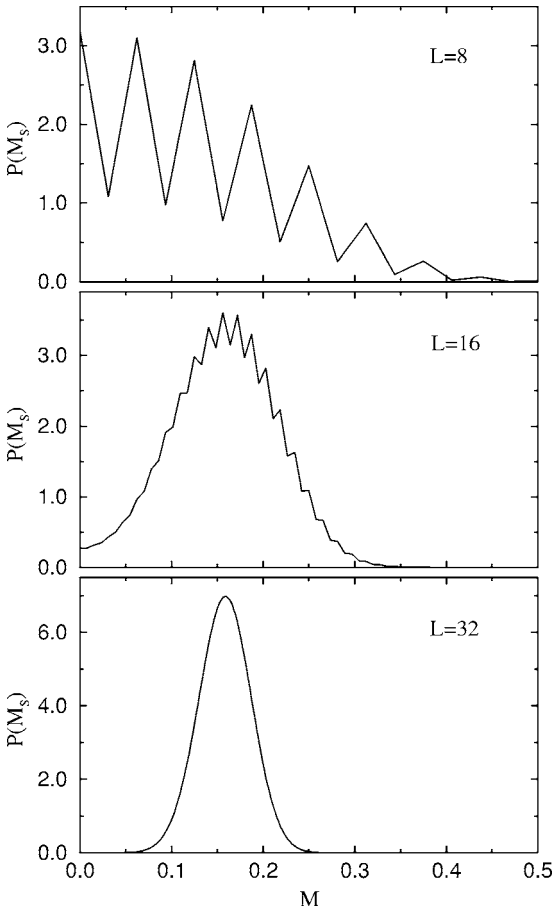

FIG. 15. Distribution of the staggered magnetization at $K/J=32$, $K/T=32$.

certainty that the transition is continuous, and in particular we do not know the intrinsic dynamic exponent z of the quantum critical point. In principle we should increase the inverse temperature $\beta=J/T$ according to $\beta\sim L^z$ as the lattice size is increased. Here we show results obtained with $\beta=L$. Figure 17 shows the integrated autocorrelation time, defined as

$$\tau[Q]=\frac{1}{2}+\sum_{t=1}^{\infty}A[Q](t), \tag{44}$$

for various lattice sizes and $K/J=7.91$. To calculate $\tau[Q]$, autocorrelation functions were measured to large Monte Carlo times ($10^2\lesssim t_{\max}\lesssim 10^3$ MC steps) until clean exponentially decaying behavior was observed. An exponential "tail" was then fitted to $A[Q](t)$ for $t_{\max}<t<\infty$ to complete the sum in Eq. (44). The resulting data of Fig. 17 have relatively large error bars for large L, that are not illustrated, however, because they are associated with uncertainties due to the way (44) is evaluated. Fits to the integrated autocorrelation data of the form $\tau\propto L^{z'}$ are consistent with a $z'\approx 2$, but this result is affected by some uncertainty because the asymptotic behavior may not yet have set in. These results again show that the multi-branch updates do not have significant enough favorable effects to include them until larger K/J.

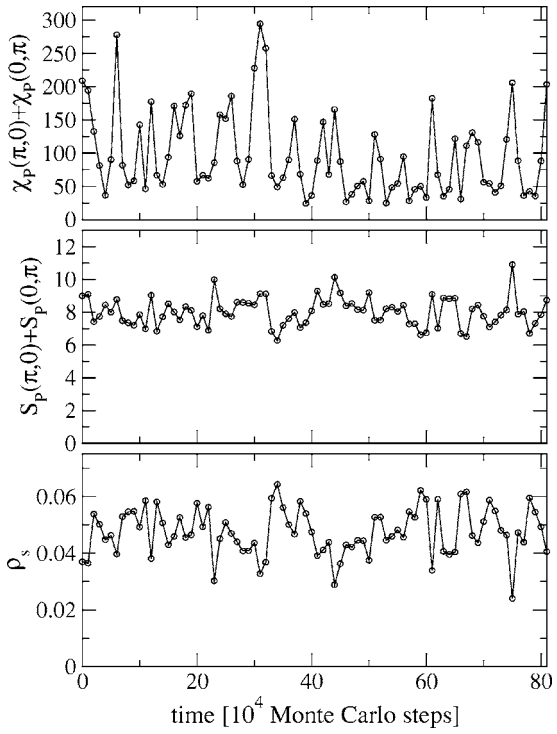

FIG. 16. Bin averages for the superfluid stiffness, the stripe structure factor, and the stripe susceptibility, for an $L=96$ lattice at $K/J=7.91$ and inverse temperature $K/T=64$. Each point represents an average over 10^4 Monte Carlo steps.

IV. DIAGONAL PLAQUETTE INTERACTIONS

In general, diagonal terms can be added to the Hamiltonian Eq. (3) without the development of a new directed-loop algorithm; only the exit probability tables change, due

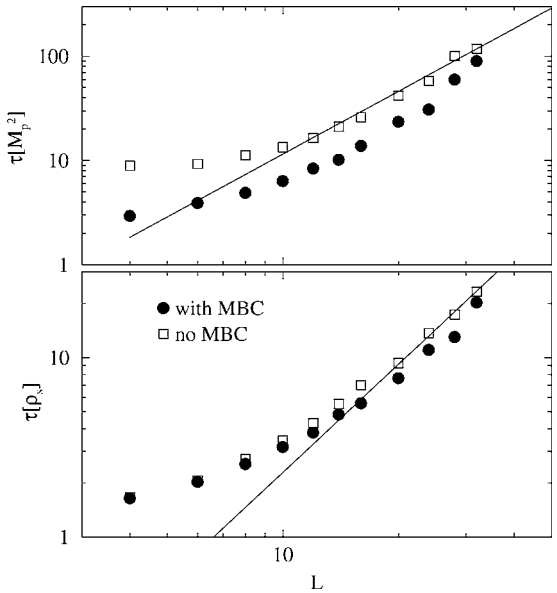

FIG. 17. Integrated autocorrelation times, Eq. (44), for the superfluid stiffness (bottom) and the squared plaquette structure factor (top) at $K/J=7.91$. The solid lines show $\tau\propto L^2$. Error bars are not shown but are significant for the largest three lattice sizes.

to the modified weights of the relevant diagonal (C) vertices illustrated in Fig. 5 (and symmetry related sets). We here consider three different diagonal terms: (i) one which enhances or suppresses staggered ("flippable" by the K term) plaquettes, (ii) a uniform external magnetic (Zeeman) field, and (iii) a staggered field.

A. Flippable-plaquette interaction

The full spin Hamiltonian including the flippable-plaquette interaction is

$$H = -J\sum_{\langle ij\rangle} B_{ij} - K\sum_{\langle ijkl\rangle} P_{ijkl} - V\sum_{\langle ijkl\rangle} Q_{ijkl}, \tag{45}$$

where the bond (B_{ij}) and plaquette (P_{ijkl}) operators are defined in Eqs. (1) and (2) and Q_{ijkl} is 1 or 0 for flippable and nonflippable plaquettes, respectively, or

$$Q_{ijkl} = (1/2 + S_i^z)(1/2 - S_j^z)(1/2 + S_k^z)(1/2 - S_l^z) + (1/2 - S_i^z) \times (1/2 + S_j^z)(1/2 - S_k^z)(1/2 + S_l^z).$$

This V interaction is interesting as it produces an exactly soluble (Rokhsar-Kivelson [35]) point at $J=0$ and $-K=V$, and is similar to the term employed in quantum dimer models [3] (see also Ref. [4]). Hence, its usefulness in making a connection between numerical and analytical studies of microscopic Hamiltonians is immediately obvious.

To solve the directed-loop equations in the presence of a diagonal interaction such as the V term, the general procedure is simply to identify, and modify, the relevant sets of directed-loop equations which include the vertex weighted by V. Here, the diagonal term $H_{1,a}$ of Eq. (11) becomes $H_{1,a}=CI_{ijkl}+VQ_{ijkl}$. In the SSE formalism, these diagonal matrix elements are represented as C vertices, each vertex having a weight given by Eq. (15). The modified vertices of interest here are denoted

$$W^V = \langle\downarrow\uparrow\downarrow\uparrow|H_a|\downarrow\uparrow\downarrow\uparrow\rangle = \langle\uparrow\downarrow\uparrow\downarrow|H_a|\uparrow\downarrow\uparrow\downarrow\rangle = V + C, \tag{46}$$

where we have represented the plaquettes of the basis state $|\alpha\rangle$ by a list of the spin states in the order $ijkl$ corresponding to Fig. 1(a). The directed-loop equations that are relevant to this diagonal term are related to those illustrated in Fig. 5, but clearly only the closed sets that contain fully staggered vertices are affected by V. The set shown in Fig. 5 does not have any such vertices and hence the corresponding directed-loop solution is the same as with $V=0$. In Fig. 18 we show a closed set that is affected by V. Here we have included the bounce processes because they can no longer be completely excluded. The directed-loop equations for this set are written as

$$v_{11} + v_{12} + v_{13} + v_{14} = W_1 = C,$$

$$v_{21} + v_{22} + v_{23} + v_{24} = W^V = V + C,$$

$$v_{31} + v_{32} + v_{33} + v_{34} = W_3 = J/2,$$

$$v_{41} + v_{42} + v_{43} + v_{44} = W_4 = J/2, \tag{47}$$

where W_1, W_3, and W_4 are the same as those given before in Eq. (16). In order to solve these equations, we use the same

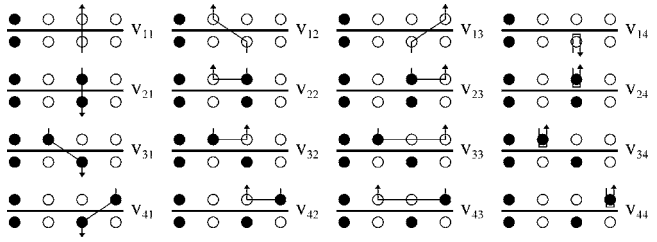

FIG. 18. A closed set of C and J vertex paths for which the corresponding directed-loop equations are different for $V=0$ and $V\neq 0$. A second set of vertex paths—the spin reverse of the one shown here—also gives the same directed-loop solution.

detailed balance requirements, Eq. (17), and symmetry arguments as previously to constrain the equations and produce a unique solution. Our choice of symmetry conditions here correspond to

$$v_{12} = v_{13},$$

$$v_{22} = v_{23},$$

$$v_{34} = v_{44}. \tag{48}$$

Two forms of the solutions are needed in order to ensure positive-definite vertex weights for all choices of parameters. The first solution is valid for small couplings, $|V| \leqslant J$, and can be formulated without the undesirable bounce processes (the right-hand column):

$$v_{11} = C - J/2 + V/2, \quad v_{12} = J/4 - V/4, \quad v_{13} = J/4 - V/4, \quad v_{14} = 0,$$

$$v_{21} = C - J/2 + V/2, \quad v_{22} = J/4 + V/4, \quad v_{23} = J/4 + V/4, \quad v_{24} = 0,$$

$$v_{31} = J/4 - V/4, \quad v_{32} = J/4 + V/4, \quad v_{33} = 0, \quad v_{34} = 0,$$

$$v_{41} = J/4 - V/4, \quad v_{42} = J/4 + V/4, \quad v_{43} = 0, \quad v_{44} = 0. \tag{49}$$

where we see that the constant C must be greater than $J/2 - V/2$ to ensure that v_{11} remains positive. However, in order to satisfy the requirement that a_{11} is positive for vertex-path sets not affected by the V term, one should set $C > J/2$ for the case $V>0$. For $V<0$, one must in addition ensure that the weight W^V in Eq. (47) remains positive, requiring a constant $C > J/2 + |V|/2$. Note that in the limit $V \to 0$, this equation set is equal to the directed-loop equations previously obtained in Eq. (18). Clearly, when $|V| > J$, a different form of the solutions must be constructed in order to ensure that each vertex weight stays positive. In the case $V > J > 0$, a nonzero bounce probability $v_{24}=V-J$ must be included. A convenient form of the solution in this case is then

$$v_{11} = C, \quad v_{12} = 0, \quad v_{13} = 0, \quad v_{14} = 0,$$

$$v_{21} = C, \quad v_{22} = J/2, \quad v_{23} = J/2, \quad v_{24} = V - J,$$

$$v_{31}=0, \quad v_{32}=J/2, \quad v_{33}=0, \quad v_{34}=0,$$

$$v_{41}=0, \quad v_{42}=J/2, \quad v_{43}=0, \quad v_{44}=0, \tag{50}$$

where the bounce process is turned on slowly, i.e., linearly with $V-J$, ensuring a small bounce probability in the algorithm for a moderate range of V larger than the exchange. However, it is clear that the bounce process v_{24} becomes negative for negative V (i.e., $V<-J<0$) and we hence need a different solution in this case. Again, we use a solution that turns the bounce processes on slowly, but in this case two nonzero bounces are required:

$$v_{11}=C+J-2|V|, \quad v_{12}=J/2, \quad v_{13}=J/2, \quad v_{14}=2|V|-2J,$$

$$v_{21}=C+J-2|V|, \quad v_{22}=0, \quad v_{23}=0, \quad v_{24}=|V|-J,$$

$$v_{31}=J/2, \quad v_{32}=0, \quad v_{33}=0, \quad v_{34}=0,$$

$$v_{41}=J/2, \quad v_{42}=0, \quad v_{43}=0, \quad v_{44}=0. \tag{51}$$

This last equation set imposes the requirement that $C>2|V|-J$. In Eqs. (49)–(51), the actual exit probabilities for the directed-loop algorithm are obtained in the usual way by dividing the matrix elements by the vertex weights; $P_{ij}^{v}=v_{ij}/W_i$, where W_i is the relevant matrix element.

Note again that when implementing a diagonal interaction such as the V term, the only change required in the simulation code, relative to the pure J-K model, is the probability weights of only the specific relevant vertex paths affected. In the case above for the plaquette V term, only the vertex set shown in Fig. 18, and the related set with the other staggered vertex, will use the solutions outlined in Eqs. (49)–(51). All other C to J vertex sets which do not contain fully staggered diagonal vertices will use the original solution Eq. (18).

B. Uniform magnetic field

Perhaps the simplest extension of the J-K Hamiltonian (3) is the addition of an external magnetic field. A diagonal Zeeman field h coupling to the z components of the $S=1/2$ spins is of particular physical importance, as it cants the magnetization away from the zero-magnetization state, or dopes the system away from half filling in the boson language [11]. The possibility of deconfined quantum critical points occurring between superfluid and insulating states at commensurate fillings other than one-half is also currently a question of interest [36]. The Hamiltonian under study is now

$$H=-J\sum_{\langle ij\rangle}B_{ij}-K\sum_{\langle ijkl\rangle}P_{ijkl}-h\sum_{i}S_i^z, \tag{52}$$

where we restrict $h>0$. The diagonal term $H_{1,a}$ of Eq. (11) is modified to include the effects of the field,

$$H_{1,a}=\frac{h}{4}(S_i^z+S_j^z+S_k^z+S_l^z)+CI_{ijkl}, \tag{53}$$

where this term now produces different matrix elements depending on the spins S_i^z,S_j^z,S_k^z,S_l^z, with an associated vertex weight Eq. (15). We can ensure that each weight will remain positive by adjusting C; in particular, we write $C=h/2+\epsilon$, where $\epsilon>0$ is typically a small constant. Representing the relevant plaquette of the state $|\alpha\rangle$ by a list of the spin states, we can calculate the weights of the 16 C vertices using Eq. (53). The results are summarized in Table II.

TABLE II. The weight factors for the diagonal vertices in the uniform J-K model.

	$\langle S_i^zS_j^zS_k^zS_l^z\|H_a\|S_i^zS_j^zS_k^zS_l^z\rangle$	Weight factor
W_1^h	$\langle\uparrow\uparrow\uparrow\uparrow\|H_a\|\uparrow\uparrow\uparrow\uparrow\rangle$	$h+\epsilon$
W_2^h	$\langle\downarrow\uparrow\uparrow\uparrow\|H_a\|\downarrow\uparrow\uparrow\uparrow\rangle$	$3h/4+\epsilon$
W_2^h	$\langle\uparrow\downarrow\uparrow\uparrow\|H_a\|\uparrow\downarrow\uparrow\uparrow\rangle$	$3h/4+\epsilon$
W_2^h	$\langle\uparrow\uparrow\downarrow\uparrow\|H_a\|\uparrow\uparrow\downarrow\uparrow\rangle$	$3h/4+\epsilon$
W_2^h	$\langle\uparrow\uparrow\uparrow\downarrow\|H_a\|\uparrow\uparrow\uparrow\downarrow\rangle$	$3h/4+\epsilon$
W_3^h	$\langle\uparrow\uparrow\downarrow\downarrow\|H_a\|\uparrow\uparrow\downarrow\downarrow\rangle$	$h/2+\epsilon$
W_3^h	$\langle\uparrow\downarrow\downarrow\uparrow\|H_a\|\uparrow\downarrow\downarrow\uparrow\rangle$	$h/2+\epsilon$
W_3^h	$\langle\downarrow\downarrow\uparrow\uparrow\|H_a\|\downarrow\downarrow\uparrow\uparrow\rangle$	$h/2+\epsilon$
W_3^h	$\langle\downarrow\uparrow\downarrow\uparrow\|H_a\|\downarrow\uparrow\downarrow\uparrow\rangle$	$h/2+\epsilon$
W_3^h	$\langle\uparrow\downarrow\uparrow\downarrow\|H_a\|\uparrow\downarrow\uparrow\downarrow\rangle$	$h/2+\epsilon$
W_3^h	$\langle\downarrow\uparrow\uparrow\downarrow\|H_a\|\downarrow\uparrow\uparrow\downarrow\rangle$	$h/2+\epsilon$
W_4^h	$\langle\uparrow\downarrow\downarrow\downarrow\|H_a\|\uparrow\downarrow\downarrow\downarrow\rangle$	$h/4+\epsilon$
W_4^h	$\langle\downarrow\uparrow\downarrow\downarrow\|H_a\|\downarrow\uparrow\downarrow\downarrow\rangle$	$h/4+\epsilon$
W_4^h	$\langle\downarrow\downarrow\uparrow\downarrow\|H_a\|\downarrow\downarrow\uparrow\downarrow\rangle$	$h/4+\epsilon$
W_4^h	$\langle\downarrow\downarrow\downarrow\uparrow\|H_a\|\downarrow\downarrow\downarrow\uparrow\rangle$	$h/4+\epsilon$
W_5^h	$\langle\downarrow\downarrow\downarrow\downarrow\|H_a\|\downarrow\downarrow\downarrow\downarrow\rangle$	ϵ

In addition, with the Hamiltonian Eq. (52), the off-diagonal plaquette operators $H_{2,a}$ to $H_{6,a}$ in Eq. (11) remain unmodified. In this case, there are now four unique sets of directed loop equations for $C\rightarrow C$ and $C\rightarrow J$ vertices that are not related by trivial symmetry operations.

The first closed set of C and J vertex paths is illustrated in Fig. 5, with weights a_{ij} which now also should include the bounce processes a_{i4} left out in the figure. If we recall that the open circle in Fig. 5 denotes a spin down, or $S^z=-1/2$, then the directed-loop equations corresponding to this set are now modified from Eq. (16) to read

$$a_{11}+a_{12}+a_{13}+a_{14}=W_5^h=\epsilon,$$

$$a_{21}+a_{22}+a_{23}+a_{24}=W_4^h=h/4+\epsilon,$$

$$a_{31}+a_{32}+a_{33}+a_{34}=W_3=J/2,$$

$$a_{41}+a_{42}+a_{43}+a_{44}=W_4=J/2. \tag{54}$$

We use the same detailed balance Eq. (17) and symmetry arguments Eq. (48) as previously to constrain the equation set and produce a unique solution. For fields $h<4J$, we can obtain a solution which contains no bounce processes,

$$a_{11}=h/8-J/2+\epsilon, \quad a_{12}=J/4-h/16, \quad a_{13}=J/4-h/16, \quad a_{14}=0,$$

$$a_{21}=h/8-J/2+\epsilon, \quad a_{22}=J/4+h/16, \quad a_{23}=J/4+h/16, \quad a_{24}=0,$$

$$a_{31} = J/4 - h/16, \quad a_{32} = J/4 + h/16, \quad a_{33} = 0, \quad a_{34} = 0,$$

$$a_{41} = J/4 - h/16, \quad a_{42} = J/4 + h/16, \quad a_{43} = 0, \quad a_{44} = 0, \tag{55}$$

where, to keep the element a_{11} positive definite, we require $\epsilon \geqslant J/2 - h/8$. Again, for $h > 4J$, the form of the solutions must change in a nontrivial way in order to keep each vertex weight positive. This requirement produces a nonzero bounce process a_{24}, which together with the other weights gives the high-field solution

$$a_{11} = \epsilon, \quad a_{12} = 0, \quad a_{13} = 0, \quad a_{14} = 0,$$

$$a_{21} = \epsilon, \quad a_{22} = J/2, \quad a_{23} = J/2, \quad a_{24} = h/4 - J,$$

$$a_{31} = 0, \quad a_{32} = J/2, \quad a_{33} = 0, \quad a_{34} = 0,$$

$$a_{41} = 0, \quad a_{42} = J/2, \quad a_{43} = 0, \quad a_{44} = 0. \tag{56}$$

The second independent closed set of vertex weights for the Hamiltonian Eq. (52) is obtained by taking the spin reverse of the closed set illustrated in Fig. 5. The resulting directed-loop equations then contain the fully polarized vertex in Table II, and are written as

$$c_{11} + c_{12} + c_{13} + c_{14} = W_1^h = h + \epsilon,$$

$$c_{21} + c_{22} + c_{23} + c_{24} = W_2^h = 3h/4 + \epsilon,$$

$$c_{31} + c_{32} + c_{33} + c_{34} = W_3 = J/2,$$

$$c_{41} + c_{42} + c_{43} + c_{44} = W_4 = J/2. \tag{57}$$

This set is solved in the same way as set a above, employing analogous conditions for detailed-balance and vertex symmetries. The result is two sets of vertex weights; the first, for $h < 4J$, is

$$c_{11} = 7h/8 - J/2 + \epsilon, \quad c_{12} = J/4 + h/16, \quad c_{13} = J/4 + h/16, \quad c_{14} = 0,$$

$$c_{21} = 7h/8 - J/2 + \epsilon, \quad c_{22} = J/4 - h/16, \quad c_{23} = J/4 - h/16, \quad c_{24} = 0,$$

$$c_{31} = J/4 + h/16, \quad c_{32} = J/4 - h/16, \quad c_{33} = 0, \quad c_{34} = 0,$$

$$c_{41} = J/4 + h/16, \quad c_{42} = J/4 - h/16, \quad c_{43} = 0, \quad c_{44} = 0, \tag{58}$$

where clearly, to keep $c_{11} > 0$, we require $\epsilon \geqslant J/2 - 7h/8$. We see that this solution is similar in form to the low-field solution for vertex set a, Eq. (55). However, the c_{11} and c_{21} terms are modified, and also the other nonzero terms have the opposite sign of h (i.e., if $a_{ij} = J/4 \pm h/16$, then $c_{ij} = J/4 \mp h/16$). The other solution corresponds to the large-field case $h > 4J$, and requires the inclusion of a nonzero weight for the bounce process c_{14},

$$c_{11} = \epsilon + 3h/4, \quad c_{12} = J/2, \quad c_{13} = J/2, \quad c_{14} = h/4 - J,$$

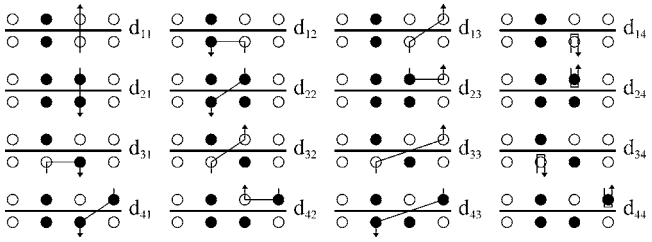

FIG. 19. A closed set of C and J vertex paths used in solving the directed-loop equations for the uniform-field J-K-h model.

$$c_{21} = \epsilon + 3h/4, \quad c_{22} = 0, \quad c_{23} = 0, \quad c_{24} = 0,$$

$$c_{31} = J/2, \quad c_{32} = 0, \quad c_{33} = 0, \quad c_{34} = 0,$$

$$c_{41} = J/2, \quad c_{42} = 0, \quad c_{43} = 0, \quad c_{44} = 0. \tag{59}$$

Again, the c_{11} and c_{21} terms are modified by the different vertex sets, and in addition the nonzero bounce process has moved to c_{14} from a_{24} in Eq. (56).

The third independent closed set of vertex weights does not include the fully spin-up or spin-down matrix elements of the previous two, sets a and c. The diagrammatic representation is therefore not trivially related to these previous cases, and is illustrated in Fig. 19. In this case, the directed-loop equations are

$$d_{11} + d_{12} + d_{13} + d_{14} = W_4^h = h/4 + \epsilon,$$

$$d_{21} + d_{22} + d_{23} + d_{24} = W_3^h = h/2 + \epsilon,$$

$$d_{31} + d_{32} + d_{33} + d_{34} = W_3 = J/2,$$

$$d_{41} + d_{42} + d_{43} + d_{44} = W_4 = J/2. \tag{60}$$

While the detailed balance conditions for this equation set are the same as before, Eq. (17), it can be noted that the additional symmetry conditions Eq. (48) do not appear in the diagrams here. Although not immediately justifiable in terms of symmetry arguments, there is in general no reason why the same constraints cannot be used to solve equation set d, and therefore we will continue to use Eq. (48) as it facilitates implementation of the algorithm (although there is no guarantee that this leads to the most efficient simulation). The low-field solution ($h < 4J$) is then given by the same equation set as solution a Eq. (55) with all $d_{ij} = a_{ij}$ *except* the following:

$$d_{11} = d_{21} = 3h/8 - J/2 + \epsilon. \tag{61}$$

Here, it is quite obvious that we require $\epsilon \geqslant J/2 - 3h/8$ in order to keep all vertex weights positive. For the high-field case ($h > 4J$), we are forced to have a nonzero bounce process, and upon solving we again get an equation set similar to solution a Eq. (56), with the exception that

$$d_{11} = d_{12} = \epsilon + h/4. \tag{62}$$

The final set of vertex weights used in the uniform-field solution is obtained by taking the spin reverse of the closed set illustrated in Fig. 19, in an analogous manner to the way

that set c was obtained from set a. The result is the directed loop equations given by

$$e_{11}+e_{12}+e_{13}+e_{14}=W_2^h=3h/4+\epsilon,$$

$$e_{21}+e_{22}+e_{23}+e_{24}=W_3^h=h/2+\epsilon,$$

$$e_{31}+e_{32}+e_{33}+e_{34}=W_3=J/2,$$

$$e_{41}+e_{42}+e_{43}+e_{44}=W_4=J/2. \quad (63)$$

Again, we employ the detailed balance and symmetry conditions discussed above to find a unique low-field solution for $h<4J$, which in this case is the same as the solution set c Eq. (58) with the exception that

$$e_{11}=e_{21}=5h/8-J/2+\epsilon, \quad (64)$$

where again the bounces have been eliminated, and to get $e_{11}>0$, we need $\epsilon \geqslant J/2-5h/8$. The large-field ($h>4J$) solutions are given by the analogous set Eq. (59), with the exception that

$$e_{11}=e_{21}=\epsilon+h/2. \quad (65)$$

As before, the above four equation sets a, c, d, and e serve to uniquely define the exit probabilities, given by dividing the matrix elements by the vertex weights, e.g., $P_{ij}^a=a_{ij}/W_i$, where the values of W_i are given either by Table II above, or by the previously defined values of $W_3=W_4=J/2$. It is important, in the implementation of the directed-loop equations, that all diagonal vertices are weighted according to their proper equation set. The relation of a general C or J vertex to the proper equation set in some cases depends on the path that a loop segment takes through the vertex. For example, the vertex in a_{31} is related to d_{31}; however, the path taken by the loop in each case results in a C vertex which is weighted differently by the field. Also, we note that the common element of all of these equation sets is the constant ϵ. This ϵ must be chosen to keep all of the elements a_{11}, c_{11}, d_{11}, e_{11} and their symmetry-related weights positive definite. The critical condition comes from Eq. (55), where $a_{11}>0$ in all cases for $\epsilon \geqslant J/2-h/8$. It can be seen that, if this condition is satisfied, then all of the weights c_{11}, d_{11}, and e_{11} will automatically be positive definite, and it is therefore the ϵ that we choose in implementation of the algorithm.

C. Staggered magnetic field

The final set of directed-loop solutions that we will present in this paper is for the J-K model in a staggered Zeeman field. Motivation for this extension of the Hamiltonian comes directly from predictions in the theory of deconfined quantum criticality [1,37] and its applicability to our microscopic model. In short, a staggered Zeeman field on our spin model corresponds to a uniform Zeeman field that couples to the z component of $\hat{n}$ in the nonlinear σ model of relevance. The theory then predicts a "split" transition between the VBS and superfluid phases, with an intermediate phase with neither order (but with a "background" field-induced staggered magnetization).

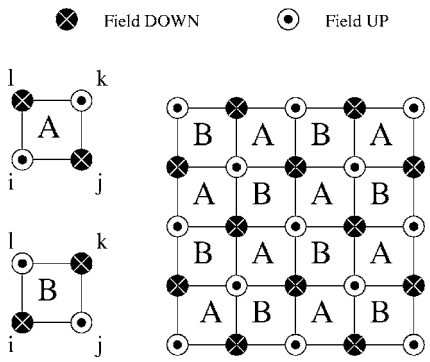

FIG. 20. Sublattice decoration of the two-dimensional square lattice, used in constructing the quantum Monte Carlo simulation of the J-K model with staggered Zeeman field.

The modified Hamiltonian is

$$H=-J\sum_{\langle ij\rangle}B_{ij}-K\sum_{\langle ijkl\rangle}P_{ijkl}-h\sum_i(-1)^{x_i+y_i}S_i^z, \quad (66)$$

where x_i and y_i are the Cartesian lattice coordinates of the ith spin, and $h>0$. The diagonal plaquette term $H_{1,a}$ of Eq. (11) is modified to include the effects of the staggered field,

$$H_{1,a}=(-1)^{x_i+y_i}\frac{h}{4}(S_i^z-S_j^z+S_k^z-S_l^z)+CI_{ijkl}, \quad (67)$$

and the other plaquette Hamiltonian terms remain unmodified. Keeping C arbitrary for now, we can easily calculate the weights for the 16 diagonal (C) vertices. The approach we take in constructing the simulation is the decorate the lattice with an A and a B sublattice in a checkerboard pattern (Fig. 20). The solution to each vertex weight in the directed-loop equations will have two components, one if the vertex happens to fall on an A plaquette, and another for the same vertex on a B plaquette (see Table III).

Turning first to the closed set of C and J diagrams, Fig. 5, we construct the directed-loop equations, which are now different from the forms Eq. (16) and Eq. (54),

$$a_{11}+a_{12}+a_{13}+a_{14}=C,$$

$$a_{21}+a_{22}+a_{23}+a_{24}=\mp h/4+C,$$

$$a_{31}+a_{32}+a_{33}+a_{34}=J/2,$$

$$a_{41}+a_{42}+a_{43}+a_{44}=J/2. \quad (68)$$

Notice that we have suppressed the explicit definition used before for the weights W in order to simplify notation. The $\mp$ sign defines the convention that the corresponding term is negative if it falls on an A plaquette, and positive if it falls on a B plaquette. We can set the bounce processes $a_{14}=a_{24}=0$ as long as $J>h/4$, giving a solution

$$a_{11}=C-J/2\mp h/8,\quad a_{12}=J/4\pm h/16,\quad a_{13}=J/4\pm h/16,\quad a_{14}=0,$$

TABLE III. The weight factors for the diagonal vertices in the staggered J-K model.

$\langle S_i^z S_j^z S_k^z S_l^z \vert H_a \vert S_i^z S_j^z S_k^z S_l^z \rangle$	A sublattice	B sublattice
$\langle\uparrow\uparrow\uparrow\uparrow\vert H_a\vert\uparrow\uparrow\uparrow\uparrow\rangle$	C	C
$\langle\downarrow\downarrow\downarrow\downarrow\vert H_a\vert\downarrow\downarrow\downarrow\downarrow\rangle$	C	C
$\langle\downarrow\uparrow\uparrow\uparrow\vert H_a\vert\downarrow\uparrow\uparrow\uparrow\rangle$	$-h/4+C$	$h/4+C$
$\langle\uparrow\downarrow\uparrow\uparrow\vert H_a\vert\uparrow\downarrow\uparrow\uparrow\rangle$	$h/4+C$	$-h/4+C$
$\langle\uparrow\uparrow\downarrow\uparrow\vert H_a\vert\uparrow\uparrow\downarrow\uparrow\rangle$	$-h/4+C$	$h/4+C$
$\langle\uparrow\uparrow\uparrow\downarrow\vert H_a\vert\uparrow\uparrow\uparrow\downarrow\rangle$	$h/4+C$	$-h/4+C$
$\langle\uparrow\downarrow\downarrow\downarrow\vert H_a\vert\uparrow\downarrow\downarrow\downarrow\rangle$	$h/4+C$	$-h/4+C$
$\langle\downarrow\uparrow\downarrow\downarrow\vert H_a\vert\downarrow\uparrow\downarrow\downarrow\rangle$	$-h/4+C$	$h/4+C$
$\langle\downarrow\downarrow\uparrow\downarrow\vert H_a\vert\downarrow\downarrow\uparrow\downarrow\rangle$	$h/4+C$	$-h/4+C$
$\langle\downarrow\downarrow\downarrow\uparrow\vert H_a\vert\downarrow\downarrow\downarrow\uparrow\rangle$	$-h/4+C$	$h/4+C$
$\langle\uparrow\uparrow\downarrow\downarrow\vert H_a\vert\uparrow\uparrow\downarrow\downarrow\rangle$	C	C
$\langle\uparrow\downarrow\downarrow\uparrow\vert H_a\vert\uparrow\downarrow\downarrow\uparrow\rangle$	C	C
$\langle\downarrow\downarrow\uparrow\uparrow\vert H_a\vert\downarrow\downarrow\uparrow\uparrow\rangle$	C	C
$\langle\downarrow\uparrow\uparrow\downarrow\vert H_a\vert\downarrow\uparrow\uparrow\downarrow\rangle$	C	C
$\langle\uparrow\downarrow\uparrow\downarrow\vert H_a\vert\uparrow\downarrow\uparrow\downarrow\rangle$	$h/2+C$	$-h/2+C$
$\langle\downarrow\uparrow\downarrow\uparrow\vert H_a\vert\downarrow\uparrow\downarrow\uparrow\rangle$	$-h/2+C$	$h/2+C$

$$a_{21} = C - J/2 \mp h/8, \quad a_{22} = J/4 \mp h/16, \quad a_{23} = J/4 \mp h/16, \quad a_{24} = 0,$$

$$a_{31} = J/4 \pm h/16, \quad a_{32} = J/4 \mp h/16, \quad a_{33} = 0, \quad a_{34} = 0,$$

$$a_{41} = J/4 \pm h/16, \quad a_{42} = J/4 \mp h/16, \quad a_{43} = 0, \quad a_{44} = 0. \tag{69}$$

Again, the upper symbol of $\pm$ or $\mp$ refers to the vertex weight on the A sublattice, and the lower symbol corresponds to the B sublattice. Note, to keep $a_{11} > 0$ on all plaquettes, we require $C \geqslant J/2 + h/8$.

Another solution for the A and B sublattices, valid for $h > 4J$, is obtained by necessarily requiring some nonzero bounce probabilities. Consider first the set of equations representing B plaquettes in Eq. (68). A simple solution can be found with a nonzero bounce, $a_{24} = h/4 - J$. Note, however,

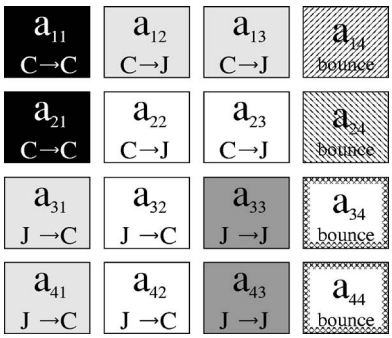

FIG. 21. Schematic representation of the closed set of C and J vertex paths used in solving the directed-loop equations for the J-K model. Blocks with the same shading represent equivalent vertex weights.

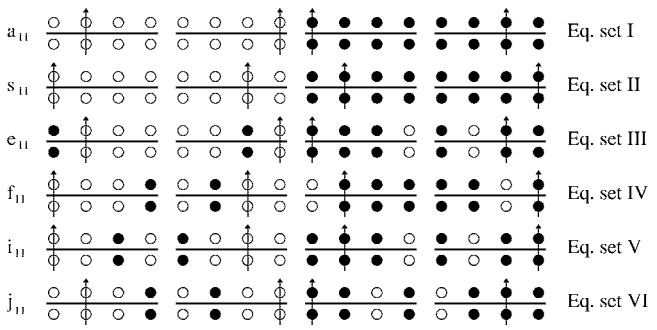

FIG. 22. Reference elements of the closed C and J vertex-path diagrams. The element letters (left) and equation set designation (right) refer to the relevant vertex weight equation set in Tables IV–IX.

that this sign in the first term in a_{24} makes this solution invalid on A plaquettes (where $h \to -h$). Thus, for $h > 4J$ on B plaquettes,

$$a_{11} = C, \quad a_{12} = 0, \quad a_{13} = 0, \quad a_{14} = 0,$$

$$a_{21} = C, \quad a_{22} = J/2, \quad a_{23} = J/2, \quad a_{24} = h/4 - J,$$

$$a_{31} = 0, \quad a_{32} = J/2, \quad a_{33} = 0, \quad a_{34} = 0,$$

$$a_{41} = 0, \quad a_{42} = J/2, \quad a_{43} = 0, \quad a_{44} = 0. \tag{70}$$

For A plaquettes, another form of the solution is needed, which is analogous to the solution Eq. (51) found for the diagonal interaction $V < -J < 0$. Setting $a_{14} = h/2 - 2J$ and $a_{24} = h/4 - J$ constrains the equations to give the solution ($h > 4J$ on A plaquettes).

$$a_{11} = C + J - h/2, \quad a_{12} = J/2, \quad a_{13} = J/2, \quad a_{14} = h/2 - 2J,$$

$$a_{21} = C + J - h/2, \quad a_{22} = 0, \quad a_{23} = 0, \quad a_{24} = h/4 - J,$$

$$a_{31} = J/2, \quad a_{32} = 0, \quad a_{33} = 0, \quad a_{34} = 0,$$

$$a_{41} = J/2, \quad a_{42} = 0, \quad a_{43} = 0, \quad a_{44} = 0. \tag{71}$$

This imposes the requirement that $C > h/2 - J$.

This outlines the basic method of constructing the directed-loop probabilities for the staggered magnetic field

TABLE IV. Vertex weight equation set I for the staggered-field J-K model. An example of the starting vertex a_{11} is illustrated in Fig. 22.

Vertex	A/B ($h < 4J$)	A ($h > 4J$)	B ($h > 4J$)
a_{11}	$C - J/2 \mp h/8$	$C + J - h/2$	C
a_{12}	$J/4 \pm h/16$	$J/2$	0
a_{14}	0	$h/2 - 2J$	0
a_{22}	$J/4 \mp h/16$	0	$J/2$
a_{24}	0	$h/4 - J$	$h/4 - J$
a_{33}	0	0	0
a_{34}	0	0	0

TABLE V. Vertex weight equation set II.

Vertex	A/B $(h<4J)$	A $(h>4J)$	B $(h>4J)$
s_{11}	$C-J/2\pm h/8$	C	$C+J-h/2$
s_{12}	$J/4\mp h/16$	0	$J/2$
s_{14}	0	0	$h/2-2J$
s_{22}	$J/4\pm h/16$	$J/2$	0
s_{24}	0	$h/4-J$	$h/4-J$
s_{33}	0	0	0
s_{34}	0	0	0

Hamiltonian. The only difficulty in completing the procedure is identifying all of the separate sets of closed vertex-path diagrams which contribute different vertex weights to the directed-loop algorithm. Instead of explicitly illustrating and solving all of these different sets in this case, we simply present the solutions in a more concise form. To begin, note that we can abbreviate the illustration of the closed sets of C and J vertex paths if we constrain the solutions to obey the same detailed balance Eq. (17) and symmetry arguments Eq. (48) as used throughout this paper. In this case, one only needs to know the upper left (reference) vertex (a_{11} in Fig. 5) in order to uniquely define the entire closed set of C to J vertex paths. The rules for constructing the closed set, as discussed in Sec. II E, can then be summarized by the schematic representation in Fig. 21, which illustrates the general relationship between the different vertex weights, and their corresponding transformations.

We can therefore easily construct an entire closed set of C and J vertex paths using Fig. 21 simply by defining the reference vertex. Following this procedure, we see that the number of unique vertex probability solution sets is narrowed down to six, unrelated by trivial symmetry operations. The reference vertices for these six unique sets are illustrated in Fig. 22. The corresponding vertex weights are summarized in the equation sets of Tables IV–IX. For example, the first reference vertex of equation set I in Fig. 22 corresponds to a_{11} of Fig. 5. The corresponding vertex weights appear in Table IV, and are equivalent to the solution sets Eqs. (69)–(71). The tables are abbreviated to include only unique weights not related by the symmetries of Fig. 21; however, the full equation sets are recovered easily by using this figure or Eqs. (17) and (48).

TABLE VI. Vertex weight equation set III.

Vertex	A/B $(h<4J)$	A $(h>4J)$	B $(h>4J)$
e_{11}	$C-J/2\pm h/8$	C	$C+J-h/2$
e_{12}	$J/4\pm h/16$	$J/2$	0
e_{14}	0	$h/4-J$	$h/4-J$
e_{22}	$J/4\mp h/16$	0	$J/2$
e_{24}	0	0	$h/2-2J$
e_{33}	0	0	0
e_{34}	0	0	0

TABLE VII. Vertex weight equation set IV.

Vertex	A/B $(h<4J)$	A $(h>4J)$	B $(h>4J)$
f_{11}	$C-J/2\mp h/8$	$C+J-h/2$	C
f_{12}	$J/4\mp h/16$	0	$J/2$
f_{14}	0	$h/4-J$	$h/4-J$
f_{22}	$J/4\pm h/16$	$J/2$	0
f_{24}	0	$h/2-2J$	0
f_{33}	0	0	0
f_{34}	0	0	0

V. DISCUSSION

In summary, we have developed in this work an extensive algorithmic framework for SSE quantum Monte Carlo simulations of the $S=1/2$ XY model with ring exchange—the J-K model—on a 2D square lattice. In addition to outlining the basic representation of the quantum mechanical partition function as a power-series expansion of plaquette operators acting on a chosen basis in the S^z representation, we have developed advanced implementations of the directed-loop and multibranch cluster updates, designed to significantly increase algorithm efficiency in various parameter regimes of the Hamiltonian. We have studied the performance of the various updating procedures using autocorrelation functions. We have also outlined modifications of the directed-loop equations to account for extensions of the J-K Hamiltonian to include diagonal (potential-energy) operators. Although several specific Hamiltonian terms are discussed, the procedure developed is sufficiently general to allow for easy extensions to other diagonal interactions.

The last step needed to provide confidence in the rather complex implementation of our directed-loop algorithms discussed here is to carry out rigorous testing. We do this by comparing SSE data with results obtained by exact diagonalization of the Hamiltonian. Table X compares ground state energies obtained in various algorithmic solution regimes of the quantum Monte Carlo schemes discussed here with exact diagonalization results for 4×4 lattices. In the simulations, the temperature T_0 was chosen sufficiently low for there to be no differences, within statistical errors, between simulations carried out at T_0 and $2T_0$. The absence of any detectable differences between the exact and SSE results to a relative statistical accuracy of $\approx10^{-5}$ illustrates the unbiased nature of these calculations.

TABLE VIII. Vertex weight equation set V.

Vertex	A/B $(h<4J)$	A $(h>4J)$	B $(h>4J)$
i_{11}	$C-J/2\pm3h/8$	$C+h/4$	$C+J-3h/4$
i_{12}	$J/4\mp h/16$	0	$J/2$
i_{14}	0	0	$h/2-2J$
i_{22}	$J/4\pm h/16$	$J/2$	0
i_{24}	0	$h/4-J$	$h/4-J$
i_{33}	0	0	0
i_{34}	0	0	0

TABLE IX. Vertex weight equation set VI.

Vertex	A/B $(h<4J)$	A $(h>4J)$	B $(h>4J)$
j_{11}	$C-J/2\mp 3h/8$	$C+J-3h/4$	$C+h/4$
j_{12}	$J/4\pm h/16$	$J/2$	0
j_{14}	0	$h/2-2J$	0
j_{22}	$J/4\mp h/16$	0	$J/2$
j_{24}	0	$h/4-J$	$h/4-J$
j_{33}	0	0	0
j_{34}	0	0	0

The SSE algorithm developed here can be extended straightforwardly to J-K models with four-spin exchange terms on other lattices. For example, implementation of the Hamiltonian on the triangular [38] and kagome [4] lattices is possible for some parameter regimes without being hampered by the sign problem. In particular, quantum Monte Carlo simulations at or near the Rokhsar-Kivelson point [35] $(J=0,\ -K=V)$ are anticipated to make explicit connection with predictions from analytical theories. Studies on these models are under way, and are expected to reveal a rich variety of ground state phenomenon.

In principle, the scheme can be extended also to multispin interactions on rings with more than four spins, for example the XY model with six-spin exchange on the pyrochlore lattice [39]. However, it is clear that the directed-loop scheme will then become quite complex, and explicit solutions of the type we have presented here may not be practical.

TABLE X. Comparison of ground state energy (per spin) of exact diagonalization and SSE quantum Monte Carlo results for various parameter values of the J-K Hamiltonian, on a 4×4 square lattice. The exchange was set to $J=1/2$, and simulations were performed with 50×10^6 Monte Carlo production steps each. The staggered field strength is represented by h_s.

K/J	V/J	h/J	h_s/J	E_{exact}	E_{QMC}
0	0	0	0	−0.5624863	−0.56249(1)
1	0	0	0	−0.6803518	−0.68034(1)
4	0	0	0	−1.1530991	−1.15311(2)
0	1/2	0	0	−0.6239222	−0.62392(1)
2	2	0	0	−1.2864452	−1.28643(2)
1	−3	0	0	−0.3983951	−0.39838(1)
1	0	2	0	−0.7434355	−0.74343(1)
5	0	6	0	−1.5000000	−1.50001(1)
4	0	0	2	−1.2547499	−1.25476(2)
1	0	0	5	−1.3859171	−1.38590(1)

ACKNOWLEDGMENTS

We would like to thank Leon Balents, Matthew Fisher, and Doug Scalapino for valuable discussions. We are grateful to Luca Capriotti for providing some exact diagonalization codes. R.G.M. acknowledges support from the Department of Energy, Grant No. DOE85-45197. A.W.S. would like to thank the Department of Physics at UCSB for hospitality during a visit. Part of the work was also carried out at the Kavli Institute for Theoretical Physics, supported under NSF Grant No. PHY99-07949.

[1] T. Senthil, A. Vishwanath, L. Balents, S. Sachdev, and M. P. A. Fisher, Science **303**, 1490 (2004).
[2] N. Shannon, G. Misguich, and K. Penc, Phys. Rev. B **69**, 220403(R) (2004); S. Sachdev, Rev. Mod. Phys. **75**, 913 (2003); O. I. Motrunich and T. Senthil, Phys. Rev. Lett. **89**, 277004 (2002); G. Misguich, B. Bernu, C. Lhuillier, and C. Waldtmann, *ibid.* **81**, 1098 (1998).
[3] R. Moessner and S. L. Sondhi, Phys. Rev. Lett. **86**, 1881 (2001).
[4] L. Balents, M. P. A. Fisher, and S. M. Girvin, Phys. Rev. B **65**, 224412 (2002); D. N. Sheng and L. Balents, Phys. Rev. Lett. **94**, 146805 (2005).
[5] R. G. Melko and D. J. Scalapino, Phys. Rev. B **71**, 094511 (2005).
[6] A. W. Sandvik, S. Daul, R. R. P. Singh, and D. J. Scalapino, Phys. Rev. Lett. **89**, 247201 (2002).
[7] A. W. Sandvik, R. G. Melko, and D. J. Scalapino (unpublished).
[8] E. Loh, D. J. Scalapino, and P. M. Grant, Phys. Rev. B **31**, 4712 (1985).
[9] K. Harada and N. Kawashima, Phys. Rev. B **55**, R11949 (1998).
[10] R. G. Melko, A. W. Sandvik, and D. J. Scalapino, Phys. Rev. B **69**, 014509 (2004).
[11] R. G. Melko, A. W. Sandvik, and D. J. Scalapino, Phys. Rev. B **69**, 100408(R) (2004).
[12] O. F. Syljuåsen and A. W. Sandvik, Phys. Rev. E **66**, 046701 (2002).
[13] A. W. Sandvik, Phys. Rev. E **68**, 056701 (2003).
[14] P. Sengupta, A. W. Sandvik, and D. K. Campbell, Phys. Rev. B **65**, 155113 (2002).
[15] A. W. Sandvik and J. Kurkijärvi, Phys. Rev. B **43**, 5950 (1991).
[16] A. W. Sandvik, J. Phys. A **25**, 3667 (1992).
[17] A. W. Sandvik, Phys. Rev. B **56**, 11678 (1997).
[18] A. W. Sandvik, Phys. Rev. B **59**, R14157 (1999).
[19] D. C. Handscomb, Proc. Cambridge Philos. Soc. **58**, 594 (1962); **60**, 115 (1964); J. W. Lyklema, Phys. Rev. Lett. **49**, 88 (1982); D. H. Lee, J. D. Joannopoulos, and J. W. Negele, Phys. Rev. B **30**, 1599 (1984); S. Chakravarty and D. B. Stein, Phys. Rev. Lett. **49**, 582 (1982).
[20] J. E. Hirsch, R. L. Sugar, D. J. Scalapino, and R. Blankenbecler, Phys. Rev. B **26**, 5033 (1982).
[21] H. G. Evertz, Adv. Phys. **52**, 1 (2003).
[22] N. Kawashima and K. Harada, J. Phys. Soc. Jpn. **73**, 1379 (2004).
[23] H. G. Evertz, G. Lana, and M. Marcu, Phys. Rev. Lett. **70**, 875 (1993).

[24] B. B. Beard and U.-J. Wiese, Phys. Rev. Lett. **77**, 5130 (1996).
[25] N. V. Prokofév, B. V. Svistunov, and I. S. Tupitsyn, Pis'ma Zh. Eksp. Teor. Fiz. **64**, 853 (1996) [JETP Lett. **64**, 911 (1996)]; Zh. Eksp. Teor. Fiz. **114**, 570 (1998) , [JETP **87**, 311 (1998)].
[26] F. Alet, S. Wessel, and M. Troyer, Phys. Rev. E **71**, 036706 (2005).
[27] K. Harada and N. Kawashima, Phys. Rev. E **66**, 056705 (2002).
[28] O. F. Syljuåsen, Phys. Rev. E **67**, 046701 (2003).
[29] L. Pollet, S. M. A. Rombouts, K. Van Houcke, and K. Heyde, Phys. Rev. E **70**, 056705 (2004).
[30] A. Dorneich and M. Troyer, Phys. Rev. E **64**, 066701 (2001).
[31] R. H. Swendsen and J. S. Wang, Phys. Rev. Lett. **58**, 86 (1987).
[32] A. W. Sandvik, R. R. P. Singh, and D. K. Campbell, Phys. Rev. B **56**, 14510 (1997).
[33] E. L. Pollock and D. M. Ceperley, Phys. Rev. B **36**, 8343 (1987).
[34] A. Cuccoli, T. Roscilde, V. Tognetti, R. Vaia, and P. Verrucchi, Phys. Rev. B **67**, 104414 (2003).
[35] D. S. Rokhsar and S. A. Kivelson, Phys. Rev. Lett. **61**, 2376 (1988).
[36] L. Balents, L. Bartosch, A. Burkov, S. Sachdev, and K. Sengupta, Phys. Rev. B **71**, 144508 (2005).
[37] T. Senthil, L. Balents, S. Sachdev, A. Vishwanath, and M. P. A. Fisher, Phys. Rev. B **70**, 144407 (2004); O. I. Motrunich and A. Vishwanath, *ibid.* **70**, 075104 (2004).
[38] L. Balents and A. Paramekanti, Phys. Rev. B **67**, 134427 (2003).
[39] M. Hermele, M. P. A. Fisher, and L. Balents, Phys. Rev. B **69**, 064404 (2004).